Study of Globular Cluster Sources using eRASS1 data

Bachelorarbeit aus der Physik

Vorgelegt von
Roman Laktionov
27. April 2021

Dr. Karl Remeis-Sternwarte
Friedrich-Alexander-Universität Erlangen-Nürnberg

Betreuerin: Prof. Dr. Manami Sasaki

Abstract

Due to the high stellar density in globular clusters (GCs), they provide an ideal environment for the formation of X-ray luminous objects, e.g. cataclysmic variables and low-mass X-ray binaries. Those X-ray sources have, in the advent of ambitious observation campaigns like the eROSITA mission, become accessible for extensive population studies.

During the course of this thesis, X-ray data in the direction of the Milky Way's GCs was extracted from the eRASS1 All-Sky Survey and then analyzed. The first few chapters serve to provide an overview on the physical properties of GCs, the goals of the eROSITA mission and the different types of X-ray sources. Afterwards, the methods and results of the analysis will be presented.

Using data of the eRASS1 survey taken between December 13th, 2019 and June 11th, 2020, 113 X-ray sources were found in the field of view of 39 GCs, including Omega Centauri, 47 Tucanae and Liller 1. A Cross-correlation with optical/infrared catalogs and the subsequent analysis of various diagrams enabled the identification of 6 foreground stars, as well as numerous background candidates and stellar sources. Furthermore, hardness ratio diagrams were used to select 16 bright sources, possibly of GC origin, for a spectral analysis. By marking them in X-ray and optical images, it was concluded that 6 of these sources represent the bright central emission of their host GC, while 10 are located outside of the GC center. For 3 out of 4 soft sources, the GC membership was verified by plotting their counterparts in optical/infrared color-magnitude diagrams of the host GC.

Contents

List of Figures

List of Tables

1 Introduction

The field of X-ray astronomy has experienced significant progress in the recent decades. Modern X-ray satellites like Chandra and XMM-Newton have equipped us with important insights into the various X-ray source populations of the Universe, while the ROSAT satelite delivered the first all-sky survey in the X-ray band. The most recent addition to our inventory of X-ray instruments is the eROSITA telescope. Launched into orbit in 2019, it aims to significantly improve our picture of the X-ray sky. After completing 8 full scans of the celestial sphere, the eROSITA All-Sky survey will be finished in 2023.
Among other sources, X-rays are emitted by hot intergalactic material, active galactic nuclei (AGNs) and X-ray binaries.
X-ray binaries categorize X-ray emitting binary star systems, e.g. main-sequence stars with a white dwarf (Cataclysmic Variables) or a neutron star companion (Low-mass X-ray binaries), as well as systems of two main-sequence-stars (active binaries) and others. Although X-ray binaries can occur in the Galactic disk, they are far more abundant in the dense cores of GCs. The high stellar density leads to a high rate of stellar encounters and thus drives the formation of these systems.
Studying observations of GCs is therefore a crucial branch of X-ray astronomy and, following the launch of the Chandra telescope, enabled the identification of over 1500 X-ray sources (Pooley, 2010). The goal of this thesis is to improve our understanding of these source populations by analyzing the X-ray sources detected in the first eROSITA scan of the celestial sphere: eRASS1.
Since the field of view of the Milky Way's GCs is typically obscured with foreground stars and background galaxies/AGNs, it is important to identify these objects and exclude them from further analysis. This can be achieved by cross-matching the X-ray sources with catalogues at other wavelengths and investigating their counterparts. Afterwards, the focus is laid upon the analysis of the GC sources. For detections with sufficient count rates, physical properties can be constrained through a spectral analysis. Furthermore, imaging software can be used to display the position of the detected sources. Color-magnitude diagrams unveil whether a source coincides with a stellar branch of the investigated GC.
During the course of this thesis, those methods will be used to acquire new information about the X-ray sources detected in the eRASS1 scan. It turns out that some GC sources represent the bright central emission of the GC, while others are located outside of the central GC region. Further analysis is required to confidently constrain the nature of these sources.

2 Globular Clusters

While the galactic disk of spiral galaxies is typically filled with a variety of objects and matter, e.g. stars, gas and dust, the outer galactic regions remain relatively empty. There is one kind of celestial bodies, however, that is almost exclusively found in the galactic halo: globular clusters (*GCs*).
GCs are compact agglomerates of old, metal-poor stars, with a density increasing from approximately 0.4 stars per cubic parsec in the outer regions to 100 - 1000 stars per cubic parsec in the central core. In total, GCs typically contain a few hundred thousand stars (Talpur, 1997). Due to their high density, GCs are strongly bound by gravity and therefore possess a symmetrical, roughly spherical shape. This lies in contrast to the asymmetrically arranged open star clusters, which are located in the galactic disk and encompass up to a few thousand stars (Frommert et al., 2007). GCs can be interpreted as an intermediate object between such open star clusters and more massive celestial bodies, e.g. nuclear star clusters and dwarf galaxies, due to the fact that they show signs of chemical evolution (Gratton et al., 2019). An optical image of the globular cluster Messier 80 is shown in Figure 2.1.

Fig. 2.1: Optical image of the globular cluster Messier 80 (*Messier 80* 2017).

Messier 80 is located in the Scorpius Constellation south to the center of the Milky

Way. It accounts for one of Milky Way's most densly populated GCs (Carretta et al., 2015).
In general, GCs are rather common, and can be found in the vicinity of nearly every sufficiently massive galaxy (Harris, 1991). The Milky Way alone is orbited by at least 147 GCs (Harris, 1997). The precise number remains unknown, however, since some Galactic regions cannot be properly observed due to obscuration by dust in the Galactic disk. According to estimates, about ten to twenty local GCs are still undiscovered (Ashman et al., 1992).
The GCs are positioned in a roughly spherical halo around the Milky Way. Many are located close to the Galactic center, but fairly few are close to the Galactic plane. A map of the GC distribution in the Milky Way is shown in Figure 2.2.

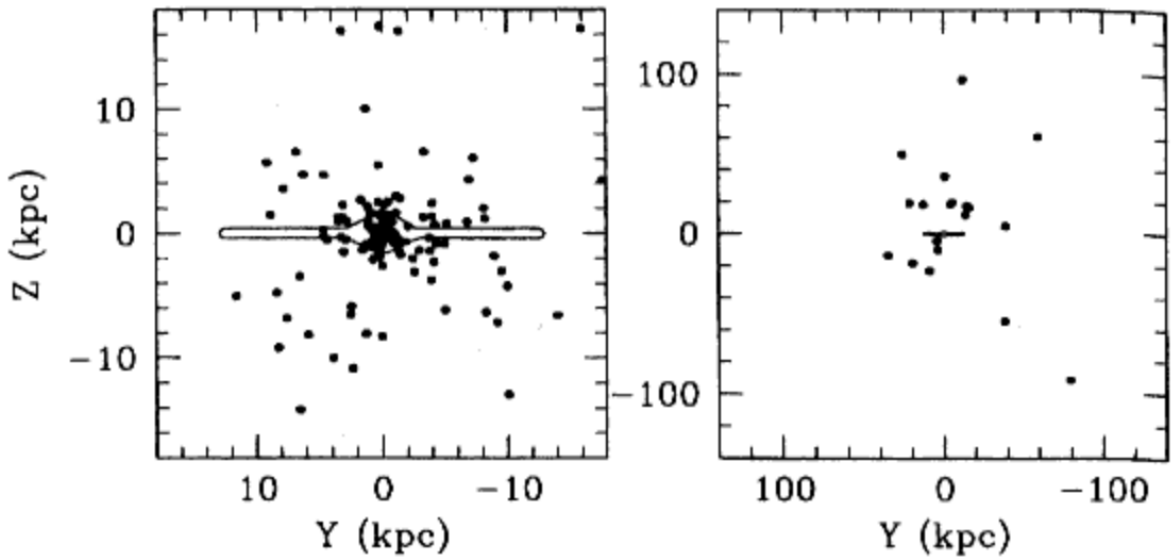

Fig. 2.2: Left: Spatial distribution of the inner GCs in the Milky Way in the YZ plane. The Galactic center is positioned at (0,0). Right: Spatial distribution of the more distant GCs. (Harris, 2001).

The largest galaxy in our cosmic neighborhood, the Andromeda Galaxy, may contain up to 500 GCs (Barmby et al., 2001). Massive elliptical galaxies, such as M87, likely account for as many as 13000 GCs (McLaughlin et al., 1994).
During the course of this section, the most important physical aspects of GCs will be reviewed.

2.1 Formation, Age, Composition

For the largest part, the formation of GCs takes place in areas of efficient star formation with exceptionally high densities, e.g. in interacting galaxies and starburst regions (Elmegreen et al., 1999). However, GCs are among the oldest objects in a galaxy. Those star formation processes presumably ended a long time ago and thereby exhausted the amount of available gas and dust. In accordance to that, observations show that they

are dust- and gas-free (Talpur, 1997). It is possible that GCs evolved from even larger collections of stars, known as super star clusters. Only very few of those objects have been discovered in the Milky Way, such as Westerlund 1 and NGC 3603 (ESO, 2005).
One of the key goals of studying GCs is to determine their age and therefore improve our understanding of their formation process in respect to the host galaxy. This is of special interest, since GCs formed before the end of reionization (12.8 Gyrs ago at $z \approx 6$) might have played a role in reionizing the Universe. It is also possible, however, that most GCs were shaped during the peak in the cosmic star formation rate at $z \approx 2$. Observations of almost 70 GCs in the Milky Way point towards the coexistence of two separate GC populations: a dominant branch of old, mostly metal-poor GCs, and a younger, higher-metallicity branch. By deriving age-metallicity relations using color-magnitude diagrams from observations of the ACS on board of the Hubble Space Telescope, those GC populations have been estimated to be approximately 12.5 Gyrs and 11.5 Gyrs old. However, due to the large uncertainties of those results, formation during the same time period cannot be ruled out. Furthermore, it is possible that the younger branch GCs have been accreted from satellite galaxies like the Sagittarius Dwarf Spheroidal Galaxy (Forbes et al., 2018).
In addition to the initial formation of the entire GCs, it is also important to consider the individual stars. To this day, it remains unclear whether the stars in a GC are generated during a single event, or across multiple formation periods over hundreds of millions of years. While the better part of stars in most GCs is at roughly the same stage of stellar evolution, some GCs feature distinct star populations. Close approaches of large molecular clouds can significantly alter their star formation history. Such events likely triggered a second round of star formation in the GCs of the Large Magellanic Cloud during their early ages (Piotto, 2009). It is also possible to attribute this kind of multiplicity to mergers of distinct GCs, especially in dense regions (Amaro-Seoane et al., 2013).
Despite possible variations in the star formation history, GCs typically exhibit old and metal-poor stars. They can be compared to stars located in the bulge of spiral galaxies. However, they are confined inside a much smaller volume (Talpur, 1997). The enormously high mass of GCs like Omega Centauri and Mayall II indicates, that some GCs embody the cores of previously consumed dwarf galaxies (Bekki et al., 2003). According to estimates, this holds true for roughly one fourth of the Milky Way's GC population (Forbes et al., 2010).

2.2 Shape and Physical Properties

While the GCs in the halo of the Milky Way and the Andromeda Galaxy are mostly spherical, those in the Small and Large Magellanic Cloud posses a more elliptical shape. Such ellipticities can result due to tidal interactions between the stars in a GC (Frenk et al., 1980). Following their formation, the stars exert a gravitational force on each other, and thereby continuously alter their motion through the GC. After the so-called *relaxation time*, their velocity has been completely renewed. In general, GCs remain gravitationally bound as long as most of the stars haven't exceeded their life span

(Benacquista, 2006).
Due to the high amount of stars concentrated in a small volume, GCs are extremely luminous. Within the Local Group, the GC luminosities can be represented by a gaussian curve. This luminosity distribution is called *the Globular Cluster Luminosity Function* and it yields an average magnitude M_{V} and a variance σ^2. For GCs in the Milky Way, those values correspond to $M_{\mathrm{V}} = -7.20 \pm 0.13$ and $\sigma^2 = 1.1 \pm 0.1$ (Secker, 1992).
In the Milky Way, NGC-5139, also referred to as *Omega Centauri*, represents the brightest GC. At a distance of 5.1 kpc from the Sun, its absolute visual magnitude of -10.24 mag appears as bright as 3.68 mag (Harris, 1997). Typically, small GCs possess masses on the order of $10^4\,\mathrm{M}_\odot$, while the largest ones exceed $10^6\,\mathrm{M}_\odot$. Omega Centauri, for instance, has a mass of $(3.55 \pm 0.03) \cdot 10^6\,\mathrm{M}_\odot$ (Baumgardt et al., 2018).
The corresponding radii can be calculated in different ways. Since the luminosity of GCs decreases, along with the star-density, with distance from the core, one can define a core-radius R_{c}, aswell as a half-light radius R_{h}. While the core-radius marks the distance, at which the apparent luminosity of the GC surface has decreased to 50 percent of the central value (Janes, 2000), the half-light radius contains the area that emits half of the total luminosity. Most GCs possess a half-light radius lower than 10 pc. However, a small fraction has exceptionally high radii, as in case of *Palomar 14*, which has a half-light radius of 25 pc (Bergh et al., 2007). Additionally, the half-mass radius R_{m}, and the tidal radius R_{t} are introduced (Buonanno et al., 1994). The half-mass radius encompasses half of the GC's mass and can be used to determine whether the GC has an unusually dense core. The tidal radius on the other hand, marks the distance from the core, at which the gravitational pull of the host galaxy becomes strong enough to separate the stars from the GC (Janes, 2000).

2.3 Color-Magnitude Diagrams

A Color-Magnitude Diagram (also called Hertzsprung-Russell diagram) represents the correlation between the absolute magnitude and the color index of a selection of stars. The color index $B-V$ of a star can be calculated by subtracting the star's magnitude in the V-band from its magnitude in the B-band. Since the stars of a GC typically formed in the same time period from the same materials, plotting the absolute magnitude of these stars over their color index will often yield a well-defined curve. The only dissimilarity between those stars is their initial mass. This lies in contrast to galactic star populations, where this sloping curve, the main-sequence, represents stars of diverse compositions, ages and masses (Sandage, 1957).

3 eROSITA Mission and X-ray Sources

3.1 eROSITA Mission

eROSITA (extended ROentgen Survey with an Imaging Telescope Array) is an X-ray instrument developed by the Max Planck Institute for extraterrestrial Physics (MPE). On July 13, 2019, it has been launched from the Baikonour cosmodrome as a part of the Russian-German Spectrum-Roentgen-Gamma (SRG) mission. The eROSITA mission started on December 13, 2019 and aims to complete an all-sky survey in energy bands between 0.2 and 8 keV by the end of 2023. An image of the eROSITA telescope is displayed in Figure 3.1.

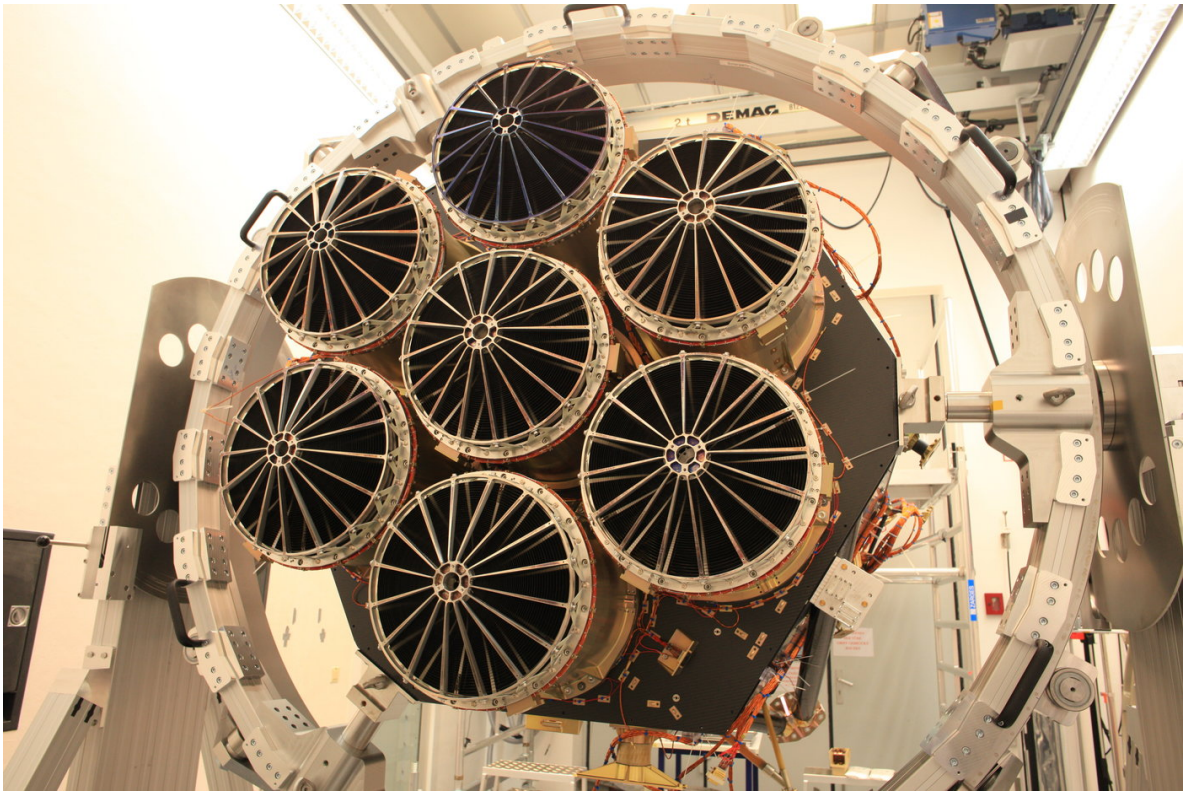

Fig. 3.1: The eROSITA X-ray telescope (Friedrich, 2019).

Alongside eROSITA, which is the primary X-ray telescope, the SRG observatory also carries the ART-XC (Astronomical Roentgen Telescope X-ray Concentrator). The ART-XC is an X-ray mirror telescope and complements the sensitivity of eROSITA at higher energies. It was developed under the lead of the Russian Space Research Institute IKI. Both instruments are attached to the *Navigator* spacecraft platform. Since

the eROSITA mission was developed under german-russian collaboration, it has been agreed to divide the observational data between the two nations. The southern hemisphere has been assigned for studies by the german side, and the nothern hemisphere for studies by the russian side.
The concept of the eROSITA instrument is an advancement of previously developed devices by the MPE, e.g. the X-ray telescope for the ROSAT X-ray satelite mission. The first complete all-sky survey with an imaging X-ray telescope was carried out by ROSAT in energy bands between 0.1 and 2.4 keV. By completing 8 complete scans of the celestial sphere, the eROSITA mission aims to increase the sensitivity of the ROSAT All-Sky Survey by a factor of 25 and to provide the first imaging survey in the hard 2.3 - 8 keV band. Each of these *eRASS* scans will last 6 months.
The primary goal of the eROSITA mission is to detect large samples of galaxy clusters up to redshifts $z > 1$. Such detections will greatly increase our understanding of the large-scale structure of the universe and provide crucial new data for the testing of cosmological models (Predehl et al., 2020). In particular, the results may constrain the rate of expansion of the Universe and deliver new insights into the nature of Dark Energy.
Galaxy Clusters can be detected due to X-ray emission from their hot intergalactic material. The eROSITA mission is expected to find 50 - 100 thousand of such galaxy clusters. Furthermore, it will enable the detection of obscured accreting black holes in nearby galaxies and millions of distant active galactic nuclei (AGNs) (*eROSITA* 2021). Those new detections will provide important new insights into the evolution of supermassive black holes (Predehl et al., 2020).
However, in addition to driving the study of cosmic structure evolution, the eROSITA mission will also greatly impact the study of Galactic X-ray source populations, such as supernova remnants, X-ray binaries, and active stars. The increased sensitivity of the eROSITA all-sky survey will allow the identification of these objects and deliver new insights into their properties.
Due to the high stellar density in GCs, they provide an ideal environment for the formation of such X-ray luminous objects. Their population of luminous low-mass X-ray binaries per unit stellar mass, for instance, is by a factor 100 higher than in the rest of the Galaxy (Homer et al., 2002). A promising method of identifying and studying X-ray luminous sources is therefore to target GC observations.

3.2 X-ray Sources

Within the framework of this study, the focus has been laid upon GC observations of the eRASS1 scan of the celestial sphere. The source selection has yielded 113 detections in the field of view of the Milky Way's GCs. It is important to note, that those findings only include sources within the southern hemisphere, which was assigned for german studies. Those detections include foreground- and background sources, as well as X-ray sources within the core and the outer regions of the GCs. The most commonly detected X-ray sources in GCs are active binaries (ABs), cataclysmic variables (CVs), millisecond Pulsars (MSPs) and low-mass X-ray binaries (LMXBs).

The goal of is this study is to identify the fore- and background sources within the 113 detections, and focus on the analysis of the GC sources (see chapter 4). The following sections serve to provide an overview over the different types of X-ray sources.

3.2.1 Foreground Sources

Foreground sources are objects that are located in the field of view of an observation, but are positioned in the foreground of the observed source. They do not belong to the GCs and are typically stars within the spiral arms of the Milky Way. Therefore they are not interesting for this study and will be eliminated from further analysis.
One way to identify foreground stars is by comparing their emission in different energy bands. Within the soft X-ray bands, their emission is typically much stronger than in harder X-ray bands. An example of this can be seen in Figure 4.18, where an X-ray emitting source is located to the right side of the GC extraction region. The soft nature of the emission indicates that the source is a foreground star.
In addition, foreground sources can be identified through bright emission in optical and infrared bands. The flux of their optical counterpart exceeds the flux of their X-ray emission (Egg, 2020).

3.2.2 Background Sources

Background sources are bright X-ray emitters that are located in the background of an observed source. This source category includes galaxies and AGNs. Although they are very distant, they still contribute to the X-ray flux. Since they don't belong to the GCs, they will also be eliminated from further analysis.
Background sources can be identified by analyzing their infrared counterparts. Radio counterparts, for instance, indicate that the source might be an AGN (Egg, 2020).

3.2.3 Globular Cluster sources

Over the last couple of decades, ambitious observation campaigns have yielded important new insights into the X-ray source populations of GCs. Einstein and ROSAT observations revealed an overabundance of low-luminosity X-ray sources ($< 10^{33}\,\mathrm{erg\,s^{-1}}$) compared to the Galactic field, while Uhuru and OSO-7 confirmed an enrichment with highly luminous X-ray sources ($> 10^{36}\,\mathrm{erg\,s^{-1}}$). Prior to the development of modern X-ray telescopes, the classification of those low-luminosity sources proved to be a big challenge. However, with the emergence of new instruments, e.g. the *Chandra X-ray observatory*, high-resolution observations enabled counterpart identifications and delivered new constraints regarding the nature of those sources (through multiwavelength analysis). By now, Chandra observations revealed at least 1500 X-ray sources in over 80 GCs. Various studies confirmed a correlation between the number of detected X-ray sources and the stellar encounter rate of a GC (Pooley, 2010).
Due to the high stellar densities in their cores, GCs often have extremely high stellar encounter rates (Bhattacharya et al., 2017) (including most of the GCs observed with

Chandra (Bassa et al., 2004)). Such conditions provide an ideal environment for the formation of various binary systems (Homer et al., 2002), including LMXBs in quiescence, CVs, ABs and MSPs. High-luminosity LMXBs were found to be orders of magnitude more common per unit mass compared to the rest of the Galaxy (Pooley, 2010). Most of these systems were formed via close stellar encounters (Bassa et al., 2004). The majority of X-ray binaries is expected to be positioned within the GCs half-mass radius (Servillat et al., 2008).

Low-mass X-ray Binaries

The brightest X-ray sources in GCs are low-mass X-ray binaries (Bassa et al., 2004). They are binary star systems composed of a donor and a neutron star or black hole accretor. The donor is either a main sequence star, a red giant or a white dwarf. The accretor is surrounded by an accretion disk due to mass transfer from the donor. The infalling matter leads to a release of gravitational potential energy in the form of X-rays. Hence, LMXBs are typically bright in X-rays, but faint in the optical. The accretion disk is the brightest part of the system (Tauris et al., 2006). In addition, some neutron star LMXBs have been observed to emit periodic X-ray bursts, which are typically by a factor 100 more luminous than their ordinary emission. Such events are categorized in Type I and Type II X-ray bursts. They are believed to occur when the accumulated matter from the donor star leads to bursting fusion reactions on the neutron star's surface. Type I bursts are a consequence of thermonuclear runaway and gradually decline after a sharp rise in luminosity. Type II bursts, on the other hand, result from gravitational potential energy release and can occur many times in a row as a quick pulse shape. Type I bursts are far more common. In fact, Type II bursts have only been detected from two sources (Lewin et al., 1993), e.g. the Rapid Burster in the GC Liller 1 (see section 4.5).
Despite the fact that GCs only contribute to $\sim 0.01\,\%$ of the total stellar mass within the Galaxy, 13 out of the $\sim$ 100 Galactic LMXBs are hosted by GCs (Zurek et al., 2009), most of them in quiescence (Pooley, 2010).
This can be explained by the fact that some dynamical LMXB formation channels might only exist in the dense cores of GCs. LMXBs can be created by exchange interactions between neutron stars and primordial binaries, the tidal capture of a main sequence star by a neutron star, or by direct collision of a neutron star with a red giant (Zurek et al., 2009). The evolution of a LMXB out of a primordial binary system on the other hand, is far less likely (Servillat et al., 2008).
It is possible that a large fraction of bright LMXBs in GCs are ultracompact X-ray binaries (UCXBs). UCXBs categorize interacting binaries that have very small binary seperations $a \simeq 10^{10}\,\mathrm{cm}$ and orbital periods $P \lesssim 1\,hr$. In the Galactic field, UCXBs only account for a small percentage of LMXBs (Zurek et al., 2009).
A subcategory of LMXB are the so-called Millisecond Pulsars (MSPs). They are pulsars with short rotational periods, and about as luminous as CVs (Bassa et al., 2004). MSPs are believed to be neutron stars from LMXB systems, that have been spinned up due to angular momentum transfer from the companion star. Such MSPs are typically observed in the radio band and can therefore by identified by their radio counterpart

(Servillat et al., 2008). In some cases, however, a portion of the MSP surface near the magnetic poles can generate X-ray radiation due to heating by relativistic particles from the magnetosphere. In addition, it is possible that those relativistic particles generate non-thermal, pulsed X-ray emission (Bhattacharya et al., 2017). High-metallicity GCs with high stellar encounter rates typically exhibit a larger abundance of MSPs (Saracino et al., 2015).

Cataclysmic Variables

In terms of brightness, LMXBs are followed by white dwarfs that are accreting material from low-mass companions (CVs). Such systems are common within the Galactic field, and even more abundant in GCs. They can either originate from primordial binaries, or result from close stellar encounters. However, a correlation between the number of faint sources and the stellar encounter rate of a GC indicates that most GC CVs are formed via close stellar encounters (Bassa et al., 2004). They can be identified by a blue, variable optical counterpart (Servillat et al., 2008).

Active Binaries

Chromospherically or magnetically active binaries are typically fainter than LMXBs and CVs. They are categorized in 3 different types. The first two are detached binary systems of either two main sequence stars, or a main sequence star and a giant/sub-giant, while the third type are contact binaries (Bassa et al., 2004). ABs can be identified by their main-sequence-like, variable optical counterparts (Servillat et al., 2008).

4 Analysis of eROSITA Data

4.1 Source Selection

The observational data of the GCs in the vicinity of the Milky Way has been acquired from *The catalogueue of Globular Clusters* (Harris, 1997). The catalogue provides a database of parameters on the mentioned GCs, including measurements for the cluster distance, luminosity, spectral types, metallicity, as well as other structural and dynamical parameters. In addition to the list of parameters, the catalogueue also provides a complete bibliography for the literature sources of every displayed quantity. The parameters are frequently updated, as new data emerges.

The goal of this section is to extract positional and dimensional data of the GCs, that are listed in the catalogue, in order to identify eRASS1 sources in the field of view of those GCs for further analysis. This was achieved by downloading an ascii-table of all 147 GCs from the VizieR website. A complete table of the 147 GCs (Table 6.1), including their IDs, as well as their position (RA = right ascension, DE = declination), their distance (R_{sun} = distance to the sun, R_{gc} = distance to the Galactic center) and their radii (R_{c} = core radius, R_{m} = half-mass radius) is displayed in chapter 6.

In order to select all of the important sources encompassed by the GCs, the area for source-selection has been defined as a circle with a radius of $5 \cdot R_{\mathrm{m}}$ around the center of the considered GC. Those regions were used to acquire fits-files containing data of the eRASS1 sources in field of view of all 147 GCs. It is important to note, though, that the available eRASS data only includes half of the sky (the other half is reserved for russian studies). The results of the source-selection yielded 113 detections, with 39 of the 147 GCs containing at least one eRASS1 source. All GCs with at least three eRASS1 sources in their field of view are listed in Table 4.1.

The acquired data includes the eRASS catalogue ID of the sources, as well as their position (RA and DE (J2000)), spatial expansion, the amount of detected X-ray counts and the count rate. The latter two are separated into three distinct energy bands, and an additional band encompassing the total number of counts. The corresponding energy ranges are displayed in Table 4.2. Those energy bands will be used to calculate the hardness ratios of the eRASS sources in the next section. The X-ray counts for each source were detected in a circle with a radius of 42 arcsec around the source position. The coordinates, counts and count rates of all 113 detections are listed in Table 6.2. Source 112 has been discarded from further analysis due to missing data.

ID	Sources
NGC 5139	16
NGC 4372	11
NGC 104	9
NGC 6397	8
NGC 5053	5
NGC 6121	5
NGC 1851	4
NGC 2808	4
NGC 6101	4
NGC 6441	3
NGC 6752	3
NGC 362	3
Terzan 2	3
Liller 1	3

Tab. 4.1: Globular Cluster ID with amount of eRASS1 sources in field of view.

X-ray band	Energy range
total	$0.2 - 5.0\,\mathrm{keV}$
soft	$0.2 - 0.6\,\mathrm{keV}$
medium	$0.6 - 2.3\,\mathrm{keV}$
hard	$2.3 - 5.0\,\mathrm{keV}$

Tab. 4.2: X-ray bands of eRASS sources.

4.2 Hardness Ratios and Count Rates

The eRASS source catalogue provides the X-ray counts, as well as the X-ray count rate of the sources for each energy band. Those values can be used to calculate the hardness ratios $\mathrm{HR_i}$:

$$\mathrm{HR_i} = \frac{B_{\mathrm{i}+1} - B_{\mathrm{i}}}{B_{\mathrm{i}+1} + B_{\mathrm{i}}} \tag{4.1}$$

where B_{i} are the total counts in the corresponding X-ray band for $i \in \{1, 2, 3\}$. Those calculations have been performed in accordance with Sasaki et al., 2018, using the counts instead of the count rates, as they provide more reliable results in the considered case.
By analyzing hardness ratios, one can acquire new information about the spectral properties of the investigated sources. They are particularly useful for the comparison of emission characteristics in different parts of the electromagnetic spectrum, since one hardness ratio contains information on two distinct bands. In the considered case, $\mathrm{HR_1}$ represents a relation between the soft ($i = 1$) and the medium ($i = 2$) band, and $\mathrm{HR_1}$ a relation between the medium and the hard ($i = 3$) band. The corresponding errors $\Delta\mathrm{HR_i}$ are defined as (Sasaki et al., 2018):

$$\Delta\mathrm{HR_i} = 2\frac{\sqrt{(B_{\mathrm{i}+1}\,\Delta B_{\mathrm{i}})^2 + (B_{\mathrm{i}}\,\Delta B_{\mathrm{i}+1})^2}}{(B_{\mathrm{i}+1} + B_{\mathrm{i}})^2} \tag{4.2}$$

In the following, the count rates of a specific energy band are denoted as C_{i}, and the corresponding errors as ΔC_{i}. Since count rate errors are not given by the eRASS source

catalogue, they must be calculated using the relation

$$\tau_{\mathrm{i}} = \frac{B_{\mathrm{i}}}{C_{\mathrm{i}}} \tag{4.3}$$

where τ_{i} represents the exposure time of the observation. Subsequently, the count rate error can be written as:

$$\Delta C_{\mathrm{i}} = \frac{\Delta B_{\mathrm{i}}}{\tau_{\mathrm{i}}} \tag{4.4}$$

The hardness ratios HR_1 and HR_2 have been calculated for each selected eRASS source with a self-written python 3 script. During the course of this thesis, the hardness ratios, as well as the count rates, will be used to acquire new information regarding the nature of the sources.

4.3 Cross-matching with other catalogues

The investigation of fluxes throughout the whole electromagnetic spectrum represents, similarly to the comparison of distinct X-ray bands, a viable method to acquire new knowledge on the analyzed sources. This is due to the fact that many types of celestial objects display characteristic emission features, which provide hints on their chemical makeup, as well as their origin. Henceforth, the goal of this section will be to cross-match the selected eRASS sources with surveys that were carried out at other wavelengths, and thereby acquire the fluxes of their counterparts. Afterwards, the new data can be used to provide new constraints on the type of object represented by the source.

catalogue	Band	Wavelength [μm]
allWISE	W1	3.4
allWISE	W2	4.6
allWISE	W3	12
allWISE	W4	22
2mass	J	1.25
2mass	K	2.17
SkyMapper	g	0.40 - 0.67
SkyMapper	r	0.48 - 0.73
gaia	g	0.3 - 1.1

Tab. 4.3: Used catalogue bands and their wavelengths (Cutri et al., 2012, *About 2MASS* 2006, *Data Release DR2. Release documentation* 2019, *Gaia DR2 Passbands* 2018).

Within the framework of this thesis, a script designated as *artemis* (written by Jonathan Knies, Dr. Karl Remeis-Observatory Bamberg), which operates upon the NWAY algorithm, will be used for the cross-matching with other catalogues. Those catalogues are based on observational data from the Wide-field Infrared Survey Explorer mission (*allWISE*), the Two Micron All Sky Survey (*2mass*), the *SkyMapper* telescope, as well

as the *Gaia* space observatory. 2mass provides counterparts in the near-infrared band, whereas the SkyMapper and Gaia catalogue provide optical counterparts. In addition, the Gaia catalogue also provides distance measurements.
The electromagnetic bands displayed in Table 4.3 are of particular interest for the following analysis and classification of the eRASS sources selected in section 4.1.

4.4 Interpreting Diagrams

To identify and study the X-ray sources located in the GCs of the Milky Way, other sources, e.g. foreground stars and background sources have to be eliminated. This was carried out by using the flux data, as well as the obtained counterparts, for the modelling of a variety of different plots. The subsequent classification was performed with an analysis of the source distribution in the resulting diagrams: discrimination of the sources in accordance to specific criteria.

4.4.1 Foreground and Background sources

As the Gaia space observatory was designed for astrometry (ESA, 2013), it acommodates for valuable distance measurements, that can be used for the identification of sources located outside of the proximity of the investigated GCs.

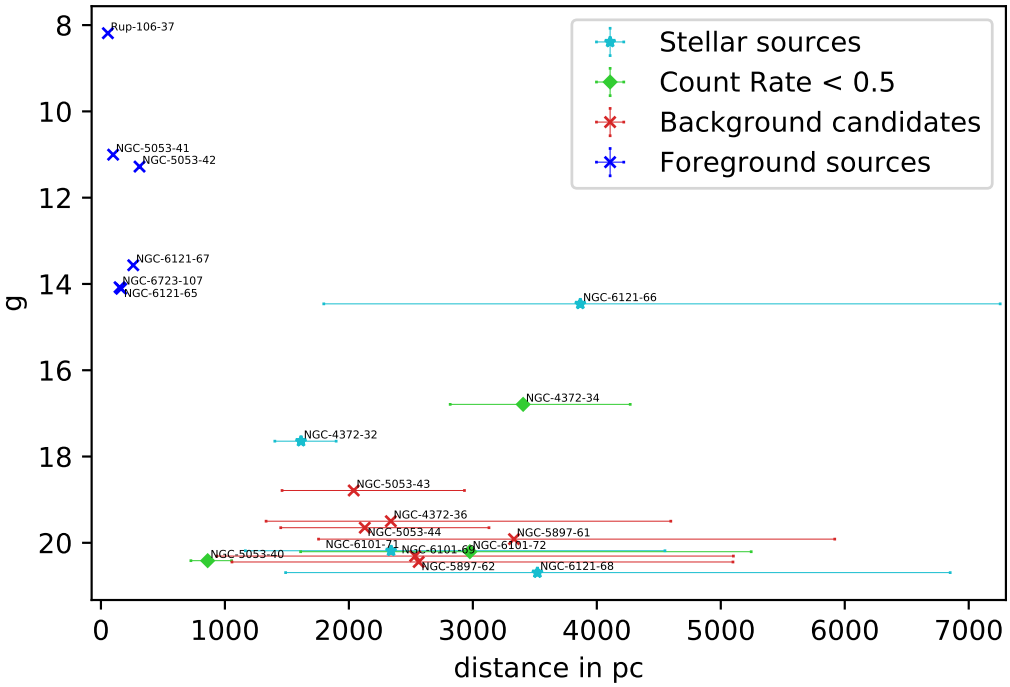

Fig. 4.1: Distance-magnitude diagram (Gaia g magnitude over distance).

The sources, for which the cross-match with the gaia catalogue was successful, have been assigned to the GC in their field of view and implemented in the distance-magnitude diagram shown in Figure 4.1. Out of the 18 sources that were matched to a source from the gaia catalogue, 16 yielded a considerably smaller distance measurement, than the corresponding GC. Despite that, the parallax distance measurements were accompanied by large uncertainties for all but six of the 18 sources. The significance of those measurements has been checked by examining whether they fulfil the four relevant criteria established by Arenou et al., 2018 and Lindegren et al., 2018.
However, due to the lack of flux data for the gaia G_{BP} and G_{RP} band, the examination did not yield meaningful results.
In conclusion, the six sources with low distance uncertainties (marked by blue crosses, seen in the upper left corner of Figure 4.1) were classified as foreground stars, whereas the remaining sources were ignored.

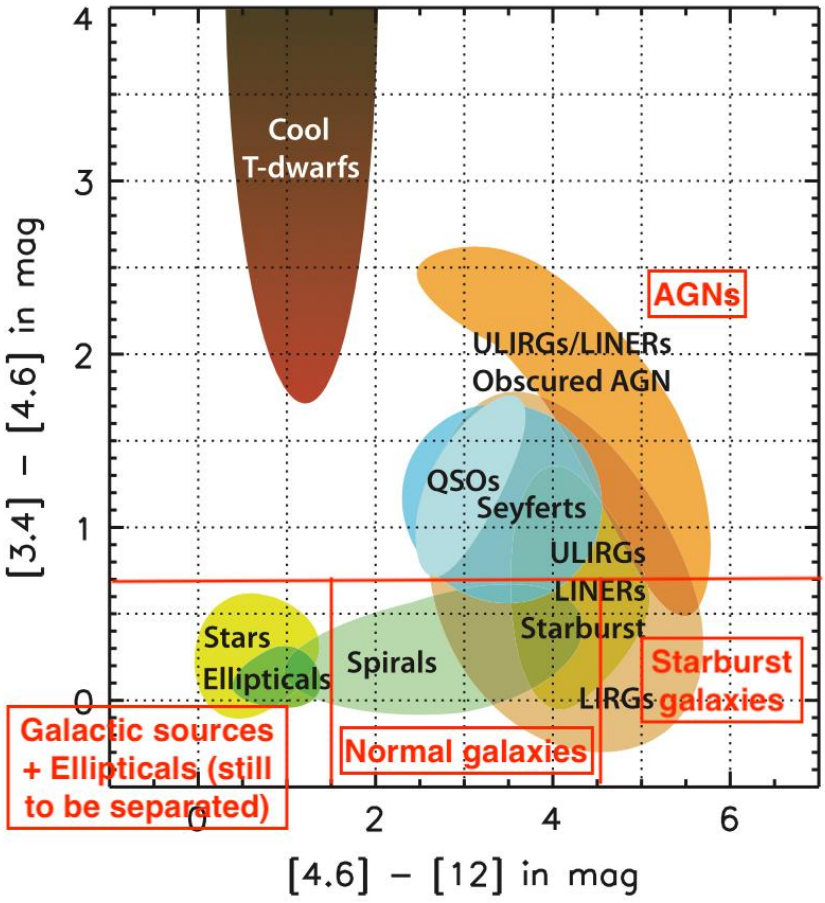

Fig. 4.2: Categorization of celestial objects according to their position in the allWISE infrared color-color diagram (W1-W2 over W2-W3) (Wright et al., 2010), red descriptions were added by Manami Sasaki.

In the next step of source identification, the eRASS sources were classified according to the categorization scheme displayed in Figure 4.2. Here, celestial bodies are separated into AGNs, Galactic sources and different kinds of galaxies according to their positioning

in an infrared color-color diagram, where the allWISE bands W1-W2 are plotted over the bands W2-W3.
The same diagram including the cross-matched allWISE magnitudes of the eRASS sources is shown in Figure 4.3. As apparent from Figure 4.2, Galactic sources and elliptical galaxies are found in the lower-left section with $W2 - W3 < 1.5$ and $W1 - W2 < 0.7$. Therefore, all sources, which fulfil these criteria, have been classified as stellar soruces (marked as light-blue stars).
AGNs on the other hand, are located in the section with $W1 - W2 > 0.7$, and starburst galaxies in the section with $W2 - W3 > 4.5$ and $W1 - W2 < 0.7$. In accordance to that, the corresponding eRASS sources have been classified as background candidates (marked as red crosses). The *normal galaxies* section can also include globular cluster sources.

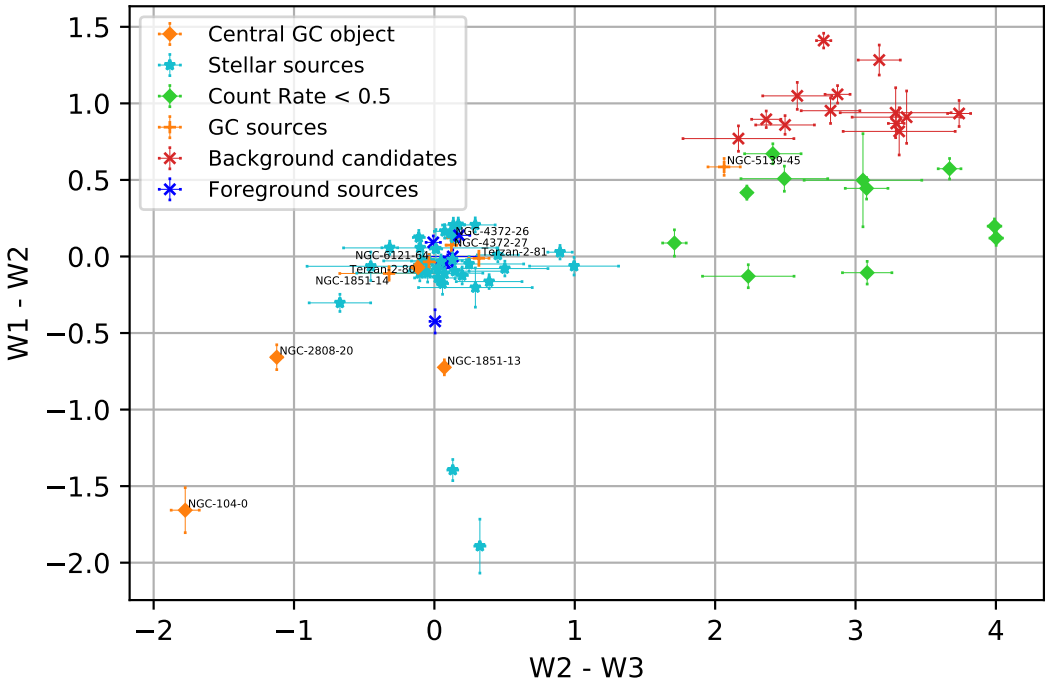

Fig. 4.3: Infrared color-color diagram (allWISE bands W1-W2 over W2-W3).

4.4.2 Hardness Ratio Diagrams

Further constraints on the nature of the sources have been acquired by plotting their hardness ratios and count rates. Since the X-ray counts are split into three distinct energy bands, only two sets of hardness ratios can be obtained: HR_1 and HR_2 (see section 4.2). These are plotted against each other in a HR_1-HR_2 diagram shown in Figure 4.4.
In addition, the plot contains six lines based on PyXspec spectral analysis models created by Sara Saeedi. Those lines represent regions of expected hardness ratio values

in dependence of the physical properties of the sources. The models include three power-law models (photon-index = 1, 2, 3) and three plasma temperature models (kT = 0.2 keV, 1.0 keV, 2.0 keV) at column densities between $N_{\mathrm{H}} = 0.01 \cdot 10^{22}\,\mathrm{cm}^{-2}$ and $N_{\mathrm{H}} = 100 \cdot 10^{22}\,\mathrm{cm}^{-2}$. However, the distribution of the sources does not show a clear correlation to the models. This leads to the conclusion, that the standard eROSITA energy bands are not useful for source-classification. In future studies, this could be dealt with by adding an additional energy band for the X-ray counts.

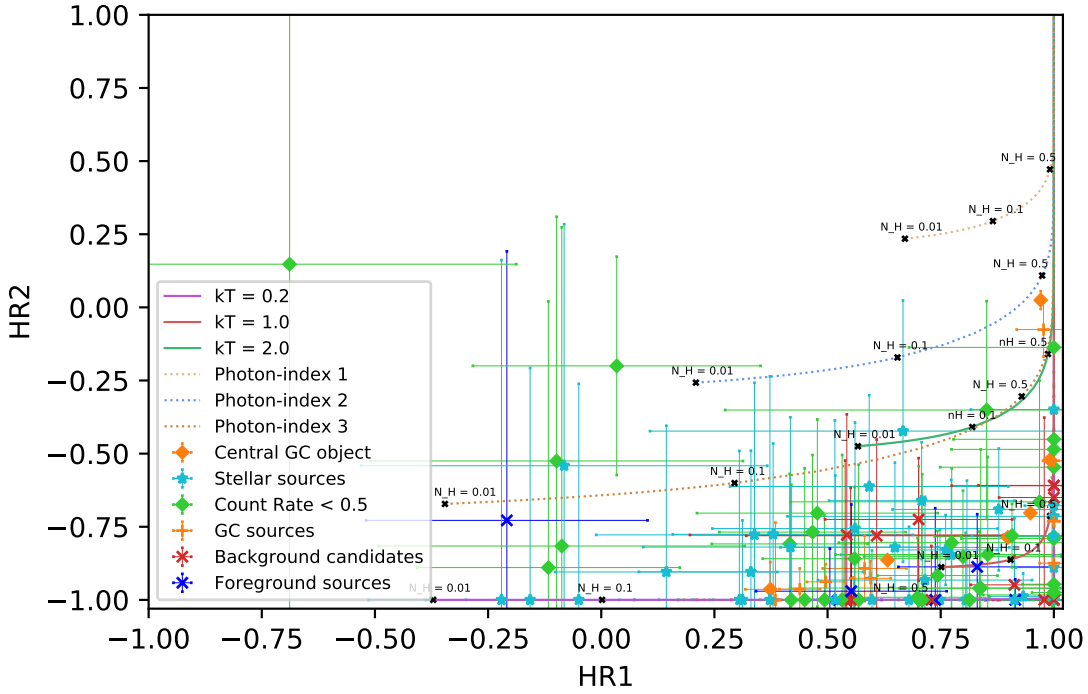

Fig. 4.4: HR-HR diagram (HR_2 over HR_1) with power-law and plasma temperature models. N_H values are given in $10^{22}\,\mathrm{cm}^{-2}$.

The figures in this section have been created under the assumption that all sources have a sufficiently high number of counts for the calculation of hardness ratios. This is not the case, however, as indicated by the sources on the bottom and right-hand edge of Figure 4.4. In order to provide a clear overview on the X-ray luminosity of the sources, the total count rate C_0 has been plotted against HR_1 and HR_2, as can be seen in Figure 4.5 and Figure 4.6, respectively. Subsequently, all sources with a total count rate $C_0 < 0.5\,\mathrm{s}^{-1}$ have been highlighted as light-green rhombuses. Although some of them are likely GC sources, their X-ray intensity is not sufficient for confident constraints on their properties. Therefore, those sources will not be further analyzed. After subtraction of the fore- and background sources, as well as the sources with insufficient X-ray counts, nine objects remained. It can be concluded, that those sources are either part of a GC or represent a central GC object. Therefore, they have been classified as GC sources and marked by orange crosses/rhombuses in all diagrams.

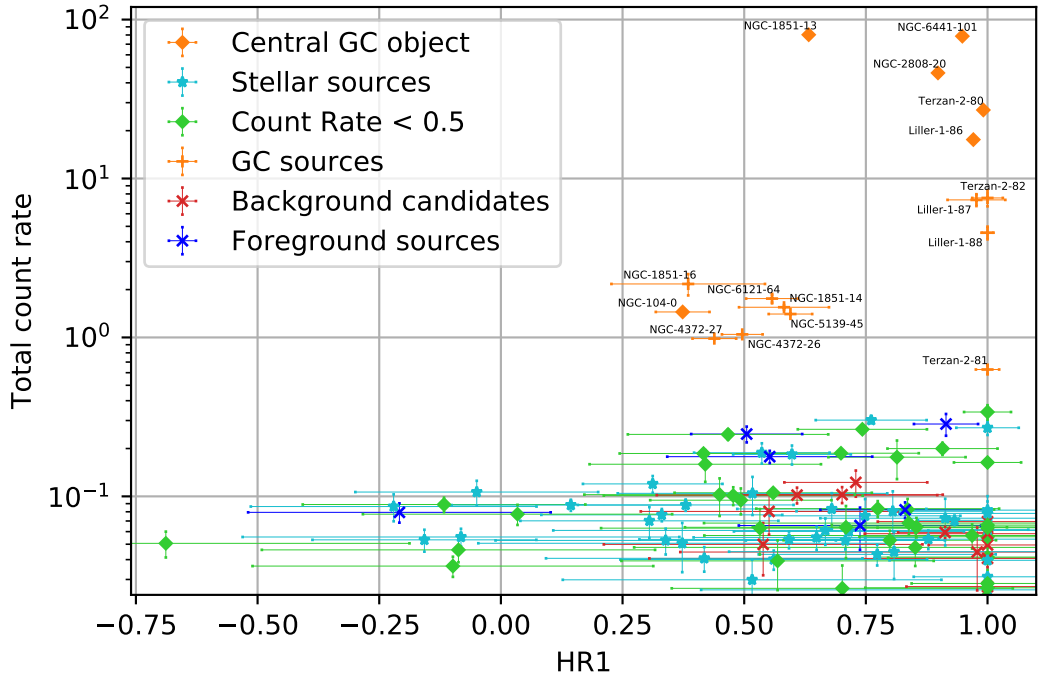

Fig. 4.5: HR-count rate diagram (C_0 over HR_1).

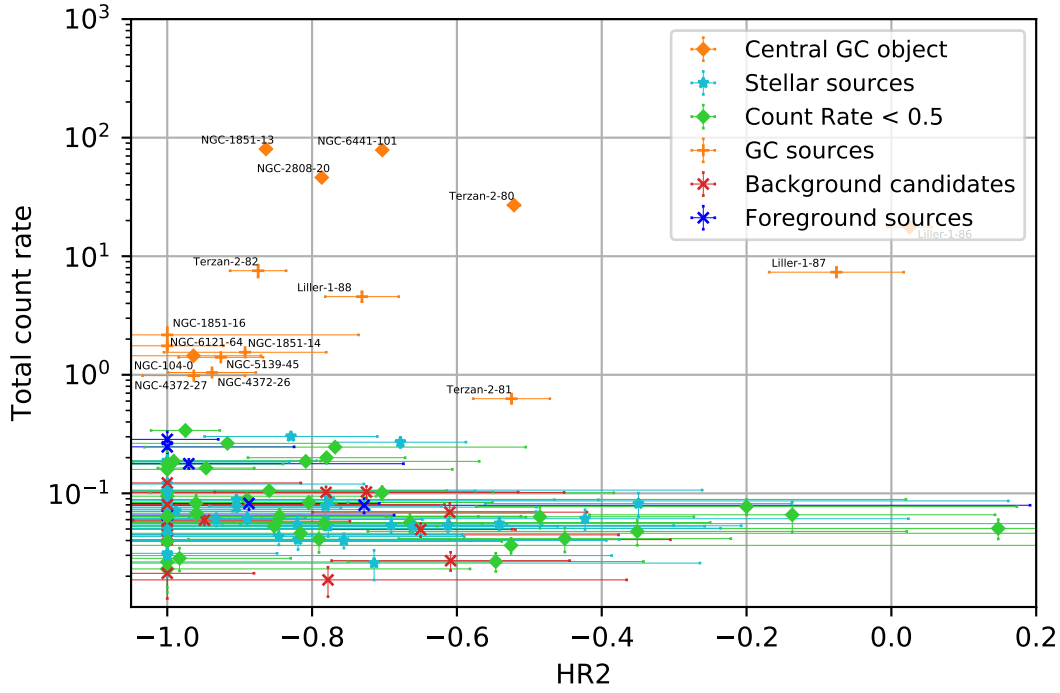

Fig. 4.6: HR-count rate diagram (C_0 over HR_2).

As apparent from Figure 4.5, the GC sources are clustered in the upper right corner of the HR_1-count rate diagram. In addition to the nine initially classified GC sources, seven stellar sources were located in the same region. Those have also been categorized as GC sources.
Afterwards, each of these sources has been assigned to their host GC and flagged with a corresponding designation. The designations have been constructed from the ID of the GC and the source. All globular cluster sources, as well as their positional data, is listed in Table 4.4. After a more detailed source-analysis in section 4.5, the presumed detection type and the contained objects have also been added to the sources in Table 4.4.

GC ID	NGC ID	Src.	RA [°]	DE [°]	Type	Contains
Liller 1		86	263.351048	-33.387020	1	LMXB
Liller 1		87	263.367080	-33.398725	2	
Liller 1		88	263.317705	-33.369826	2	
Terzan 2		80	261.886976	-30.800186	1	LMXB
Terzan 2		81	261.828809	-30.828867	2	
Terzan 2		82	261.904339	-30.789197	2	
Caldwell 73	NGC 1851	13	78.525579	-40.043858	1	LMXB & MSP
Caldwell 73	NGC 1851	14	78.511218	-40.061486	2	
Caldwell 73	NGC 1851	16	78.581367	-40.043111	2	
Melotte 95	NGC 2808	20	138.009602	-64.866835	1	LMXB & CVs
Omega Cen	NGC 5139	45	202.170112	-47.463716	2	
NGC 6441	NGC 6441	101	267.550853	-37.050205	1	LMXB & MSPs
47 Tucanae	NGC 104	0	6.010449	-72.081343	1	LMXB & others
Messier 4	NGC 6121	64	245.845533	-26.370861	2	
Caldwell 108	NGC 4372	26	186.299651	-72.450269	2	
Caldwell 108	NGC 4372	27	186.392734	-72.462313	2	

Tab. 4.4: Globular cluster sources. Type 1: central GC region, Type 2: outside of GC center.

4.5 Analysis of Globular Cluster Sources

Following the classification of the detected sources, the GC sources displayed in Table 4.4 have been further analyzed.
During the first step, optical images of the GCs have been acquired from the SkyView website (SkyView, 2021). Since the GC sources are located in the southern hemisphere, the DSS total band of the Optical:DSS survey has been chosen. Those images have then been used to plot the positions of the eRASS1 sources (small green circles with the corresponding source ID) and the source extraction region of each GC (large green circle). This was achieved through a self-written shell script operating upon the image tool *SAOImageDS9*. The results show the extent of the GC (five half-mass radii), as well as the position/distance of the sources in respect to the GC core. In addition, it can be seen whether the X-ray sources coincide with noticeably bright emission in the optical band. The images are presented during the course of this section.

Afterwards, the focus was laid onto the X-ray band. Using observational data from the eRASS1 mission (acquired by Sara Saeedi), RGB X-ray images were created in a similar way to the optical images. These images provide a more detailed insight into the distribution of X-ray emission within the GCs and the X-ray emission characteristics of the eRASS1 sources. Blue marks represent emission in the soft X-ray band, red marks emission in the medium X-ray band, and green marks emission in the hard X-ray band (see Table 4.2).
The images have been used to constrain the nature of the GC sources. For detections in the central region of a GC, it can be concluded that they represent the emission of sources within the GC core. Since the cores of GCs contain a large amount of sources (on the order of $10^5 - 10^6$ sources), often including X-ray emitters like CVs, MSPs, ABs and LMXBs, it is possible that the detection is composed of the emission of a large number of sources. Detections of this type have been classified as *Type 1*, while detections outside of the central GC region have been classified as *Type 2*. Type 2 detections, which coincide with a peak in X-ray emission in the corresponding X-ray image, presumably represent a single bright X-ray source or a small number of X-ray emitting sources in close proximity to each other. However, some of the detections generated relatively high X-ray counts although they don't coincide with a peak in emission in the X-ray images. These detections are mostly located close to the GC center where the stellar density (and the amount of X-ray binaries) is still relatively high. It is therefore possible that those detections were triggered by an above-average number of bright X-ray emitters in the detection circle (with a radius of 42 arcsec) and were discarded from further analysis. The detection type of each GC source is shown in Table 4.4.

Host GC	Src. ID	Model	N_{H} $10^{22}\,\mathrm{cm}^{-2}$	kT keV	Photon-index	χ^2/DOF
Liller 1	86	tbabs(po)	$2.09^{+0.26}_{-0.24}$	-	$0.60^{+0.19}_{-0.18}$	1.03
Terzan 2	80	tbabs(po)	$1.38^{+0.12}_{-0.11}$	-	$1.96^{+0.17}_{-0.16}$	1.20
NGC 1851	13	tbabs(bb+po)	$0.05^{+0.01}_{-0.01}$	$0.30^{+0.05}_{-0.04}$	$1.54^{+0.07}_{-0.07}$	1.21
NGC 2808	20	tbabs(bb+po)	$0.16^{+0.05}_{-0.05}$	$0.55^{+0.04}_{-0.03}$	$1.15^{+0.27}_{-0.31}$	1.12
Omega Cen	45	tbabs(bb)	< 0.11	$0.39^{+0.11}_{-0.09}$	-	1.44
NGC 6441	101	tbabs(bb+po)	$0.33^{+0.05}_{-0.08}$	$0.76^{+0.31}_{-0.20}$	$1.33^{+0.31}_{-0.35}$	1.10
47 Tuc	0	tbabs(bb)	< 0.03	$0.23^{+0.03}_{-0.02}$	-	1.41
Messier 4	64	tbabs(bb)	$0.43^{+0.36}_{-0.31}$	$0.12^{+0.06}_{-0.03}$	-	1.33
NGC 4372	26	tbabs(bb)	< 0.04	$0.23^{+0.02}_{-0.02}$	-	1.02
NGC 4372	27	tbabs(bb)	< 0.09	$0.22^{+0.02}_{-0.04}$	-	1.15

Tab. 4.5: Model parameters of analyzed sources.

The next goal was the modelling of the X-ray spectra of the GC sources. After the

extraction of the eRASS1 spectra by Sara Saeedi, they were analyzed with the X-Ray Spectral Fitting Package *Xspec*. Bad channels were removed in order to minimize the errors.
The X-ray emission of the sources is expected to be predominantly generated by electrons that are accelerated in magnetic fields around a compact object (synchrotron radiation), or as thermal emission from the compact objects surface and accretion disk. The non-thermal synchrotron radiation can be modelled by a powerlaw, while the thermal emission can be described by a blackbody model. Therefore, powerlaw and blackbody models, aswell as a combination of both models, were fitted onto the spectra. The spectra with the best fitting model are presented during the course of this section. In most cases, the blackbody model has been chosen for soft sources, and a combination of the blackbody and powerlaw model for sources with a wide energy-range spectrum. The resulting parameters of the models, as well as the uncertainty of the model (χ^2 divided by the number of degrees of freedom), are listed in Table 4.5.
N_{H} characterizes the column density in the field of view of the source, kT the temperature of the source and Photon-index the index of the powerlaw model. Initial fit values for N_{H} have been derived from *NASA's HEASARC Column Density Tool* 2021.
The spectra of the sources NGC-104-0, NGC-6121-64, NGC-4372-26 and NGC-4372-27 are softer than the rest. Therefore, those sources are discussed in greater detail. 2mass near IR color-magnitude diagrams, as well as SkyMapper optical color-magnitude diagrams have been plotted for the host GCs of those sources in order to further constrain the origin of those sources.
In addition to the analysis of the eRASS1 sources, a search for previously detected X-ray sources in the host GCs has been conducted. The most interesting findings have been marked in the corresponding X-ray images by yellow and orange circles. The details are presented in separate sections for each GC. In most cases, the designations for the previously detected X-ray sources are equivalent to those in their respective studies. At the end of this section, Table 4.7 summarizes the probable nature of those sources.

Liller 1

With a distance of only 0.8 kpc to the center of the Milky Way, the high-density GC ($\log \rho_{\mathrm{core}} = 7.85\,\mathrm{M}_{\odot}/\mathrm{pc}^3$) (Baumgardt et al., 2018) Liller 1 is one of the few GCs positioned within 1 kpc from the Galactic center. In addition, it is located in close proximity to the Galactic plane. The high stellar density in this Galactic region leads to a large foreground extinction of Liller 1 observations. Therefore, the available observational data is very shallow. However, the properties of Liller 1 suggest that it provides an optimal environment for the formation of exotic objects (CVs, LMXBs, MSPs). The creation of such objects is likely catalyzed by dynamical interactions within the GC, e.g. stellar collisions. In addition to being one of the most metal-rich GCs in the Galactic buldge after Terzan 5, Liller 1 has the highest stellar encounter rate of all star clusters in the Galaxy. However, the only identified exotic object in the core of Liller 1 is the LMXB *MXB 1730-335*, also called *Rapid Burster*. It is the only LMXB in the Galaxy that emits type I, as well as type II X-ray bursts. The position of the LMXB is marked by the yellow circle in Figure 4.7. The outburst phase lasts a few weeks and occurs

every 6 to 8 months. During that phase, the time interval between the bursts can drop down to seven seconds, with varying burst fluxes. Moreover, Homer et al., 2001 detected three further low-luminosity X-ray sources within two core-radii (quiescent LMXB candidates). Another interesting characteristic of Liller 1 is its γ-ray emission. The Large Area Telescope on board the Fermi Telescope has detected the most intense γ-ray emission from a Galactic GC in the direction of Liller 1. This is another indicator that Liller 1 hosts a large amount of MSPs (Saracino et al., 2015).

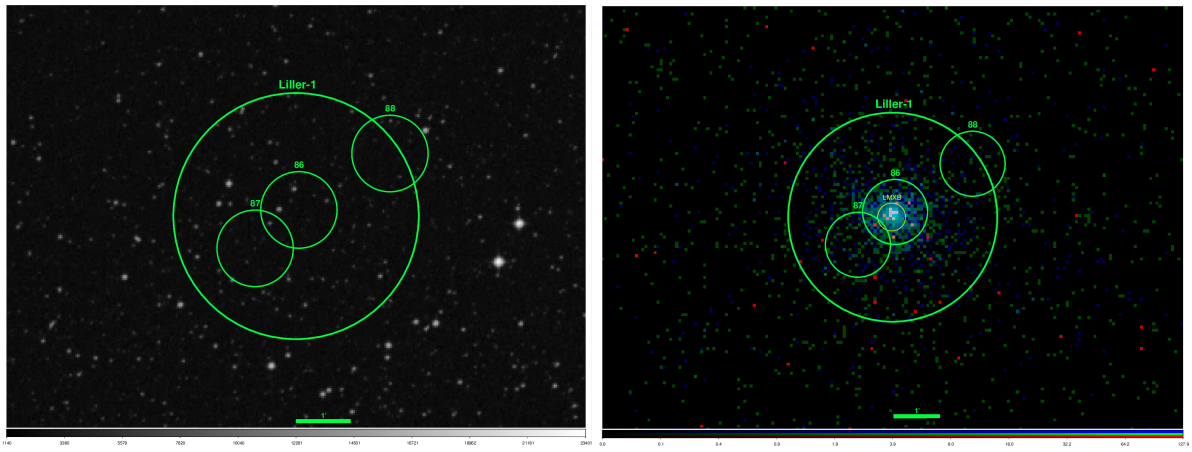

Fig. 4.7: Left: Optical image of Liller 1 (DSS total band).
Right: X-ray image of Liller 1. Blue marks represent emission in the soft X-ray band, red marks emission in the medium X-ray band, and green marks emission in the hard X-ray band. The large green circle marks a region of $5R_{\mathrm{m}}$ around the GC, the small green circles mark a $42'$ region around the eRASS1 sources. The Yellow circle marks the LMXB *MXB 1730-335*.

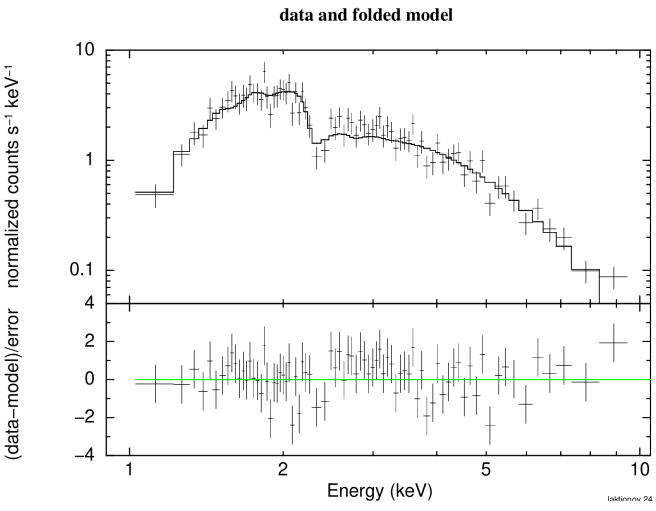

Fig. 4.8: Spectrum of Liller-1-86.

The eRASS source selection in the direction of Liller 1 has yielded three results: source 86, 87 and 88. All three out of these sources have been classified as a GC source. As apparent from the X-ray image (Figure 4.7), Source 86 encompasses bright X-ray emission in the central GC region. The LMXB *MXB 1730-335* is also located in the bright central region of the GC. It can be concluded that source 86, which generated 1949.05 counts, represents the combined X-ray emission of multiple sources in the GC core, including the emission from *MXB 1730-335*.

With 827.27 and 587.25 counts, respectively, source 87 and 88 are also relatively bright. However, neither of them coincide with a peak in emission in the X-ray image. The

detections represent the enhanced X-ray emission within an extended circle (with a radius of 42 arcsec) in close proximity to the GC center. The emission likely originates from multiple X-ray emitting sources within the encircled region.
The spectrum of source 86 is displayed in Figure 4.8. It covers a wide energy range (roughly $1 - 10\,\mathrm{keV}$). With a χ^2/DOF value of 1.03, the powerlaw-model yielded the best fit.

Terzan 2

Terzan 2 is positioned in close proximity to the Galactic center ($R_{\mathrm{gc}} = 1.6\,\mathrm{kpc}$). It is a relatively dim GC in a distance of 9.5 kpc to the sun. However, it contains the bursting LMXB *4U 1722-30*. The variable hard X-ray source has been detected with the SIGMA γ-ray telescope onboard the GRANAT satelite at energies exceeding 40 keV by Mereghetti et al., 1995. It is marked by the yellow circle in the X-ray image (Figure 4.9). Signs of quasi-periodic oscillations have been discovered in the energy range 2-8 keV at a constant level of the source flux ($1.3 \cdot 10^{-13}\,\mathrm{Jm^{-2}s^{-1}}$) (Belli et al., 1986).

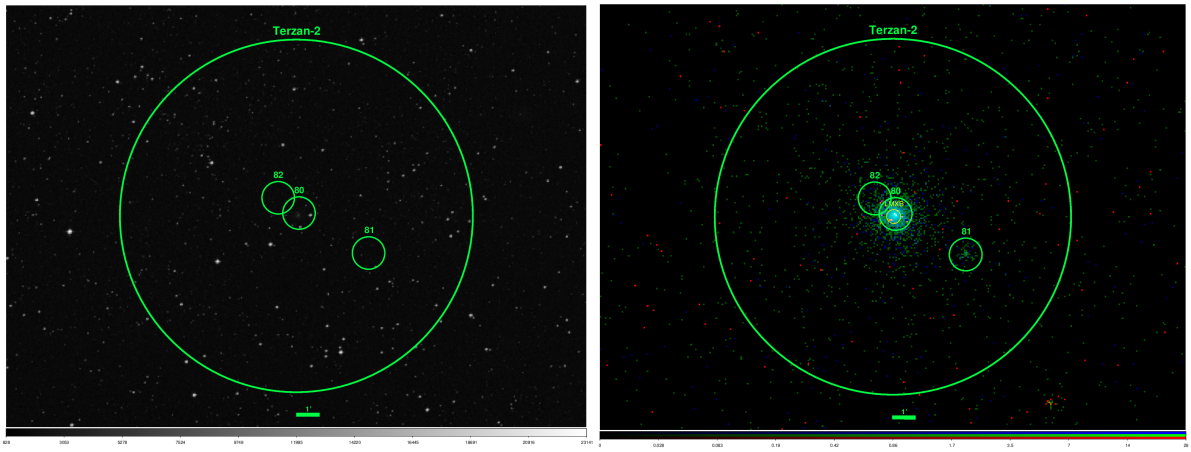

Fig. 4.9: Left: Optical image of Terzan 2 (DSS total band)
Right: X-ray image of Terzan 2 (similar to Figure 4.7), yellow circle marks the LMXB *4U 1722-30*.

All three eRASS sources in the direction of Terzan 2 (source 80, 81 and 82) have been classified as GC sources. Source 82 doesn't coincide with a peak in emission in the X-ray image. Source 81 on the other hand, encompasses a visibly brighter region in the X-ray image than the surrounding area, although the flux is relatively low (78.52 counts). It is possible that multiple X-ray emitting GC sources are concentrated in the central area of detection 81. Source 80 coincides with bright X-ray emission in the central GC region. The LMXB *4U 1722-30* is also located in the bright central region of the GC. It can be concluded that source 80 represents the combined X-ray emission of multiple sources in the GC core, including the emission of *4U 1722-30*.
The spectral analysis included source 80 and 81. However, for source 81, the number of detected counts was too low for modelling. The spectrum of source 81 is displayed

in Figure 4.11. For source 80 on the other hand, a powerlaw model yielded the best fit (χ^2/DOF = 1.20) (see. Figure 4.10).

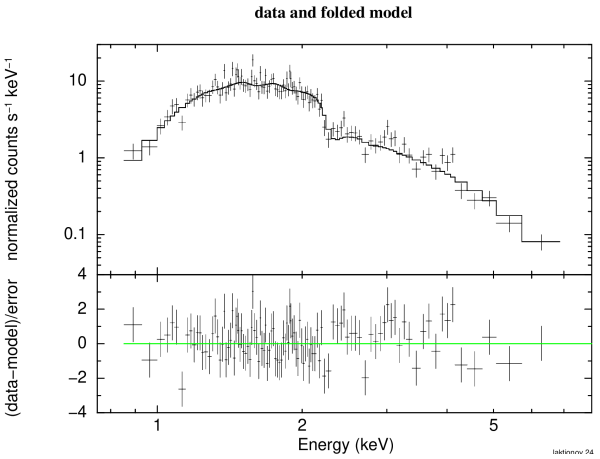

Fig. 4.10: Spectrum of Terzan-2-80.

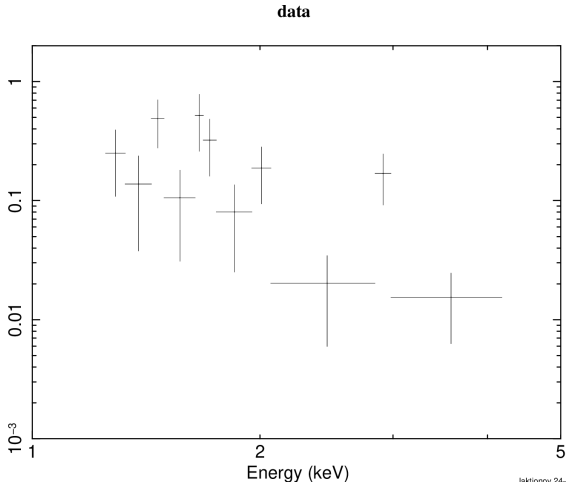

Fig. 4.11: Spectrum of Terzan-2-81.

NGC 1851

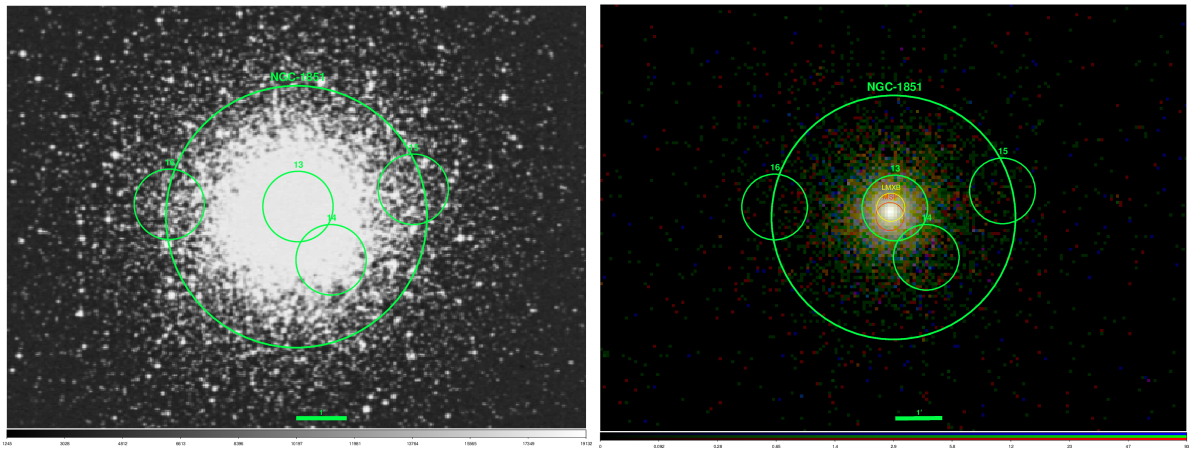

Fig. 4.12: Left: Optical image of NGC 1851 (DSS total band)
Right: X-ray image of NGC 1851 (similar to Figure 4.7), the yellow circle mark the LMXB *4U 0513-40*.

NGC 1851 is a high density GC ($\log \rho_{\text{core}} = 6.57\,\mathrm{M}_\odot/\mathrm{pc}^3$) (Baumgardt et al., 2018) located at a distance of 12.2 kpc to the Sun. It contains the LMXB *4U 0513-40*, which emits a periodic signal with $P \simeq 17$ min and amplitude $3\,\% - 10\,\%$. It is marked by a yellow circle in the X-ray image (Figure 4.12). Zurek et al., 2009 concluded that the signal is of orbital nature and thereby confirmed the source as an ultracompact X-ray binary (UCXB). It has a luminosity of $\sim 3 \cdot 10^{36}\,\mathrm{ergs}^{-1}$ (Callanan et al., 1995). In addition, NGC 1851 contains the 4.99 ms MSP *PSR J0514-4002A*. It is located in a binary system with a massive companion and a period of $P = 18.8$ d. It is marked by

an orange circle in the X-ray image. In a recent study, Ridolfi et al., 2019 analyzed upgraded Giant Metrewave Radio Telescope timing measurements of *PSR J0514-4002A* and found indications that the companion might also be a neutron star.

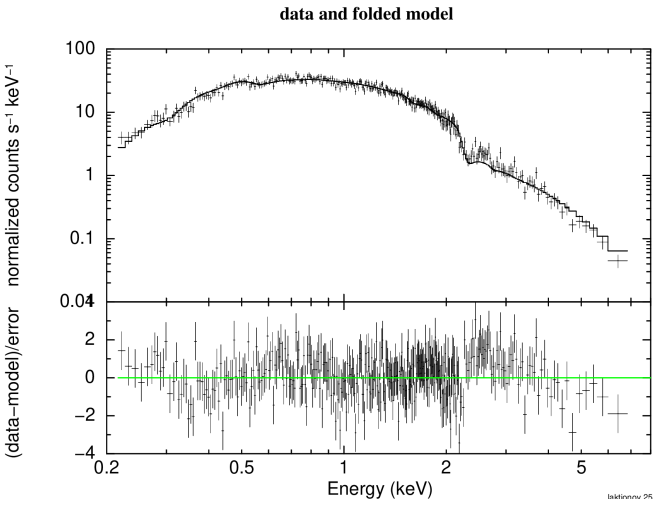

Fig. 4.13: Spectrum of NGC-1851-13.

Three out of the four eRASS sources in the field of view of NGC 1851 have been classified as GC sources: source 13, 14 and 16. Source 15 generated only 29.65 counts and is therefore too faint for further analysis. The sources 14 and 16 don't coincide with a peak in emission in the X-ray image. Source 13 on the other hand, encompasses bright X-ray emission in the central GC region. The UCXB is also located in the bright central region of the GC. It can be concluded that source 13 represents the combined X-ray emission of multiple sources in the GC core, including the emission of the UCXB.

The spectrum of source 13 is displayed Figure 4.13. It covers an energy range from 0.2 to 7 keV. Due to the soft nature of the spectrum, a blackbody component has been added to the powerlaw model.

NGC 2808

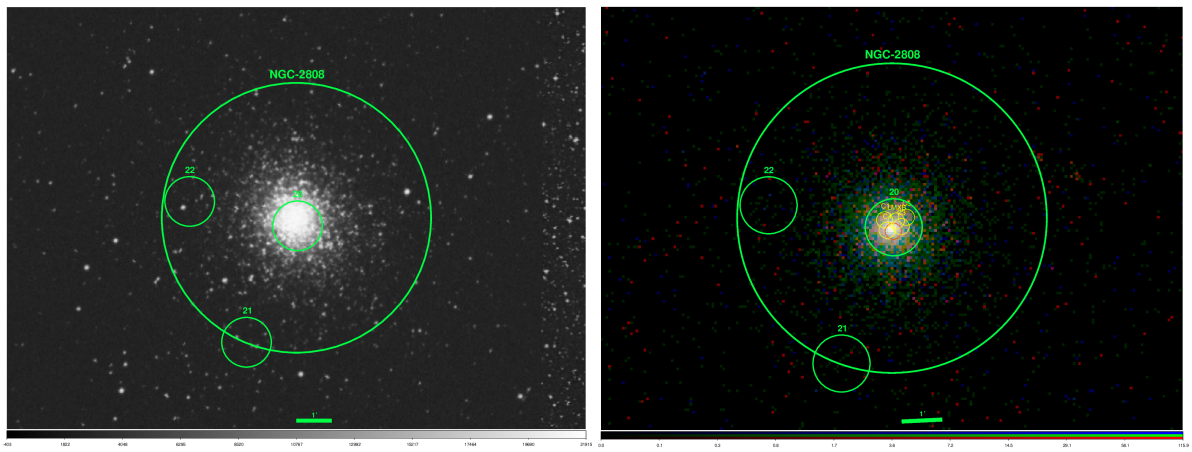

Fig. 4.14: Left: Optical image of NGC 2808 (DSS total band)
Right: X-ray image of 2808 (similar to Figure 4.7), the yellow circles mark a LMXB and four CVs discussed by Servillat et al. (2007).

NGC 2808 is a massive, high density GC ($\log \rho_{\mathrm{core}} = 4.60\,\mathrm{M}_{\odot}/\mathrm{pc}^3$) (Baumgardt et al., 2018) located in a distance of 9.3 kpc to the Sun. Servillat et al., 2008 studied XMM-

Newton observations of NGC 2808 and found five X-ray sources related to the GC. One of those sources is a quiescent neutron star LMXB candidate with a luminosity of $(2.6 \pm 0.4) \cdot 10^{32}\,\mathrm{erg\,s^{-1}}$. They further suggest that the majority of X-ray sources in the center of the GC are CVs, including the four other detected X-ray sources. The position of the LMXB and the four CVs has been marked by yellow circles in Figure 4.14.

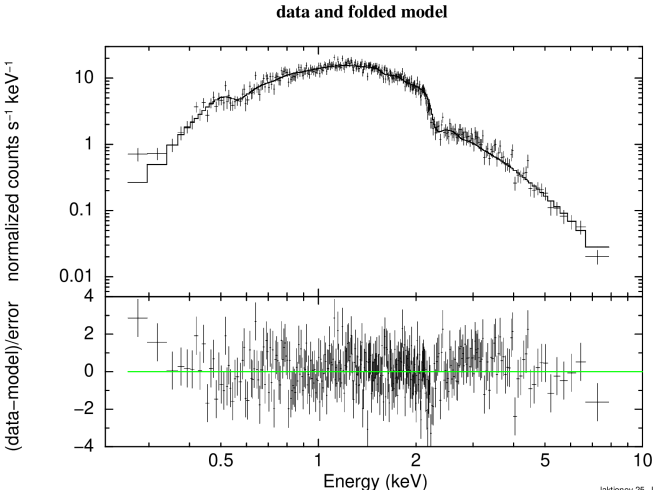

Fig. 4.15: Spectrum of NGC-2808-20.

According to estimates, the GC harbours 20 ± 10 CVs with a luminosity higher than $4.25 \cdot 10^{31}\,\mathrm{erg\,s^{-1}}$ (Servillat et al., 2008). In addition, Sanna et al., 2017 recently discovered an accreting MSP (*MAXI J0911-655*), which is part of an ultracompact binary system, in XMM-Newton and NuSTAR observations. The X-ray transient emits coherent pulsations ($P = 2.9\,\mathrm{ms}$) at a frequency of $\sim 339.97\,\mathrm{Hz}$ (Sanna et al., 2017). It is marked by an orange circle in the X-ray image.

The eRASS source selection in the direction of NGC 2808 yielded three results: source 20, 21 and 22. Source 21 and 22 don't coincide with a peak in emission in Figure 4.14. Source 20 on the other hand, encompasses bright X-ray emission in the central region of the GC. The five X-ray sources discovered by Servillat et al., 2008, as well as the MSP discovered by Sanna et al., 2017, are located in this region. It can be concluded, that source 20 represents the combined X-ray emission of multiple sources in the GC core, including the emission of the five X-ray sources discovered by Servillat et al., 2008.
The spectrum of source 20 can be seen in Figure 4.15. Due to the wide energy range of the spectrum (0.3 - 8 keV), a blackbody component has been added to the powerlaw model.

Omega Centauri

With an absolute magnitude of $M_\mathrm{V} = -10.26$, ω Cen (NGC 5139) is the most luminous GC in the Milky Way. Furthermore, it has a mass of $\sim 3 \cdot 10^6\,\mathrm{M_\odot}$ and is therefore the second most massive GC in the Local Group. It is located in a distance of 5.2 kpc to the Sun and has a core radius of $R_\mathrm{c} = 4.22\,\mathrm{pc}$ (Baumgardt et al., 2018). This results in a high stellar interaction rate (Henleywillis et al., 2018). Therefore, a large amount of exotic objects is expected to be located in ω Cen. Henleywillis et al., 2018 studied a deep X-ray survey of ω Cen observed with the ACIS-I detector onboard the Chandra X-ray Observatory. They found that 60 ± 20 X-ray sources are related to ω Cen, with ~ 30 sources being located within R_c, and another ~ 30 within $(1 - 2)\,R_\mathrm{c}$. Among those sources they identified 18 CVs and CV candidates, one quiescent LMXB and four variable stars. According to their estimations, ω Cen contains 40 ± 10 CVs

with a luminosity greater than $10 \cdot 10^{31}\,\mathrm{ergs}^{-1}$. Furthermore, 30 unidentified sources have properties like MSPs in other GCs. In addition, they've shown that the second brightest X-ray source in the GC has a CH star counterpart. CH stars are metal-poor red giants with an overabundance of carbon and s-process elements (McClure et al., 1990). Recently, Dai et al., 2020 studied Parkes radio telescope observations and found five MSPs in ω Cen. The 13 brightest X-ray sources, that were discussed in the study of Henleywillis et al., 2018, as well as the LMXB, have been marked by yellow circles in the X-ray image (Figure 4.16).

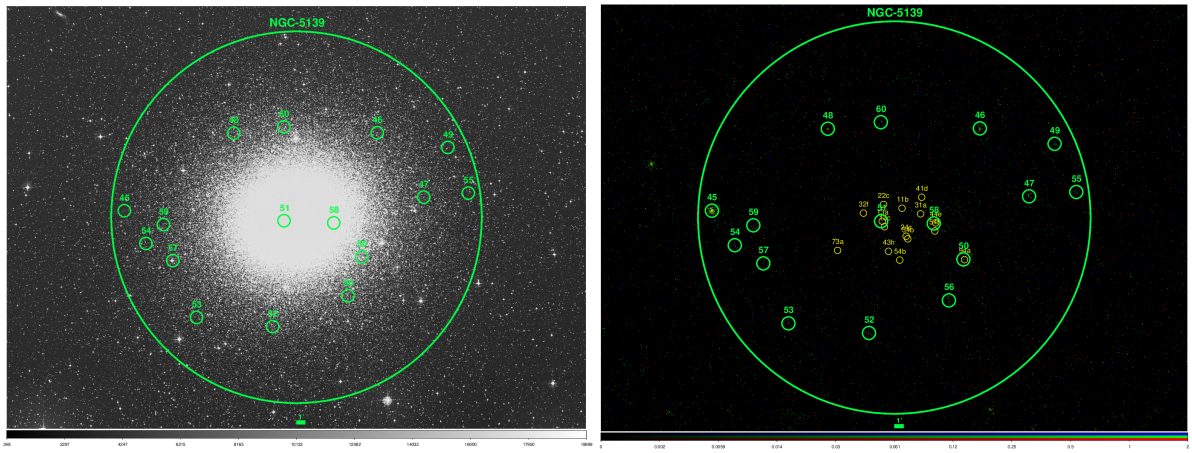

Fig. 4.16: Left: Optical image of NGC 5139 (DSS total band)
Right: X-ray image of NGC 5139 (similar to Figure 4.7), yellow circles mark the 13 brightest X-ray sources discussed by Henleywillis et al. (2018) and the LMXB.

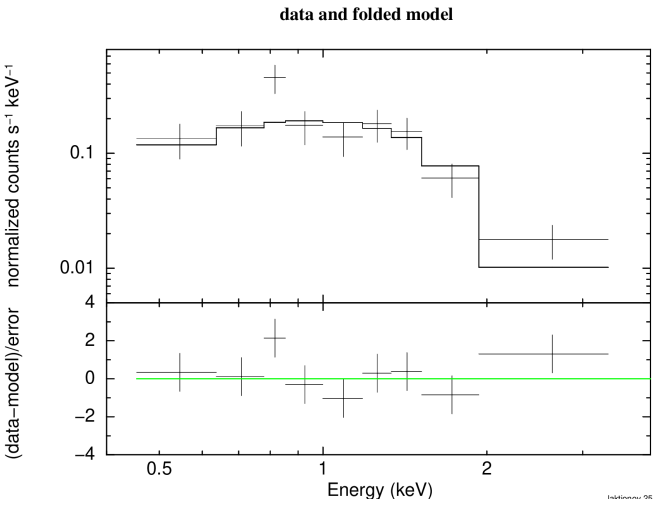

16 eRASS1 sources have been detected in the field of view of ω Cen. Most of them coincide with unusually bright spots in the X-ray image (Figure 4.16). However, only source 45 has been classified as a GC source (which is luminous enough for further analysis). With 358.61 counts, it is the brightest out of the 16 sources and is located near the edge of the five half-mass-radii extraction region. It has been classified as a type 2 detection.

Fig. 4.17: Spectrum of NGC-5139-45.

Interestingly, detection 50 coincides with the position of source 94a from the study of Henleywillis et al., 2018, which is the CH star, and detection 51 coincides with the position of source 13a (CV). Detection 58 coincides with the position of source 94a

(the LMXB). In contrast to the previously discussed GCs, the X-ray image of ω Cen does not display bright X-ray emission in the central GC region. This can be explained by ω Cen's small core density $\log \rho_c = 3.22\,M_\odot/pc^3$ (Baumgardt et al., 2018). The previously discussed GCs had much larger core densities $\log \rho_c \geq 4.60\,M_\odot/pc^3$. This high concentration of stellar sources in a small area caused bright X-ray emission. In ω Cen on the other hand, the sources are spread across a much larger central region and hence do not generate composite X-ray emission. A comparison of the GC's radii, masses and core densities can be seen in Table 4.6. In addition, the detection of bright X-ray emission depends on the behaviour of the variable sources. ω Cen hosts at least four variable stars. If these stars experienced a flare during the time of the observation, the emission might have been visible in the X-ray image.
The spectrum of source 45 is displayed in Figure 4.17. Covering an energy range of 0.5 - 3 keV, it is a very soft source and has therefore been fitted by a blackbody model.

NGC 6441

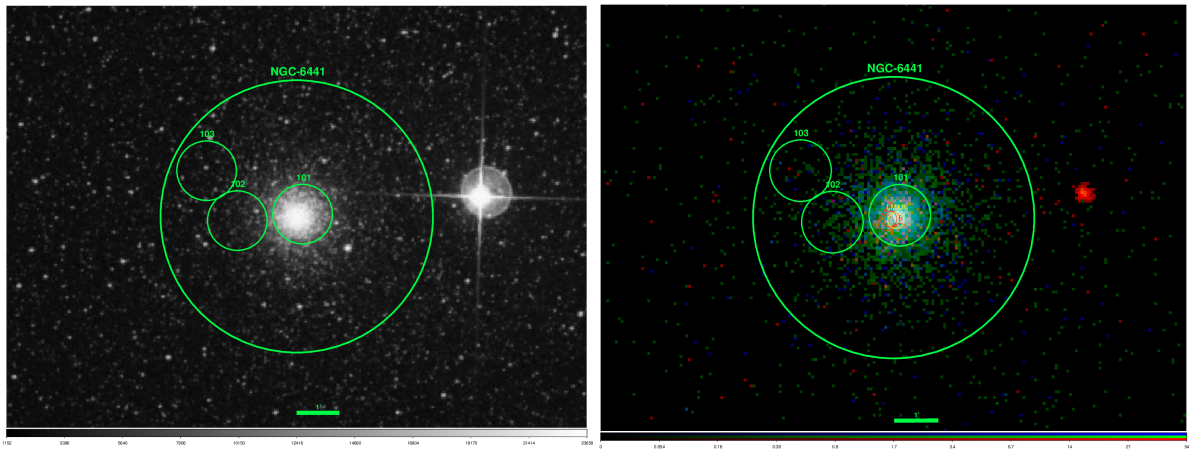

Fig. 4.18: Left: Optical image of NGC 6441 (DSS total band)
Right:X-ray image of NGC 6441 (similar to Figure 4.7), yellow circle marks the LMXB *4U 1746-37*.

NGC 6441 is a metal-rich (Caloi et al., 2007), high-density GC ($\log \rho_{core} = 5.40\,M_\odot/pc^3$) (Baumgardt et al., 2018), located close to the Galactic center ($R_{gc} = 2.1\,kpc$) in a distance of 9.7 kpc to the Sun. It contains the LMXB *4U 1746-37*, which is positioned $\sim 6''$ from the GC center (Deutsch et al., 1998) and displays periodic variability (Sansom et al., 1993b). It is marked by a yellow circle in Figure 4.18. Parmar et al., 1989 and Sansom et al., 1993a found a 5.7hr period of $\sim 5\,\%$ amplitude (Deutsch et al., 1998). This is the longest known period out of all GC X-ray sources (Homer et al., 2002).
The flux varies between $2.8 \cdot 10^{-10}$ and $17.4 \cdot 10^{-10}\,erg\,s^{-1}$ in an energy range of $2 - 11\,keV$ (Sansom et al., 1993b). In addition, Freire et al., 2008 used the Green Bank Telescope's S-band receiver and the Pulsar Spigot spectrometer to conduct a search for pulsars. They discovered 4 new MSPs in NGC 6441, out of which 2 are located in binary systems. The MSPs are marked by orange circles in the X-ray image.

The eRASS source selection in the field of view of NGC 6441 yielded three results: source 101, 102 and 103. Source 102 and 103 don't coincide with a peak in emission in the X-ray image (Figure 4.18).

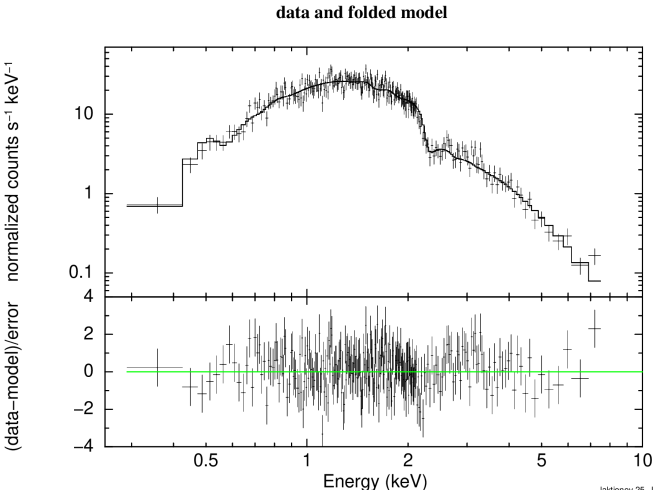

Fig. 4.19: Spectrum of NGC-6441-101, source 1.

Source 101 on the other hand encompasses bright X-ray emission in the central region of the GC. Since *4U 1746-37* is located in the core of the GC, it can be concluded that source 101 represents the combined X-ray emission of multiple X-ray sources in the GC core, including the emission of *4U 1746-37*. The spectrum of source 101 is displayed in Figure 4.19. It covers a wide energy range between 0.3 and 7 keV. Therefore, a combined powerlaw and blackbody model has been fitted onto the spectrum.

47 Tucanae

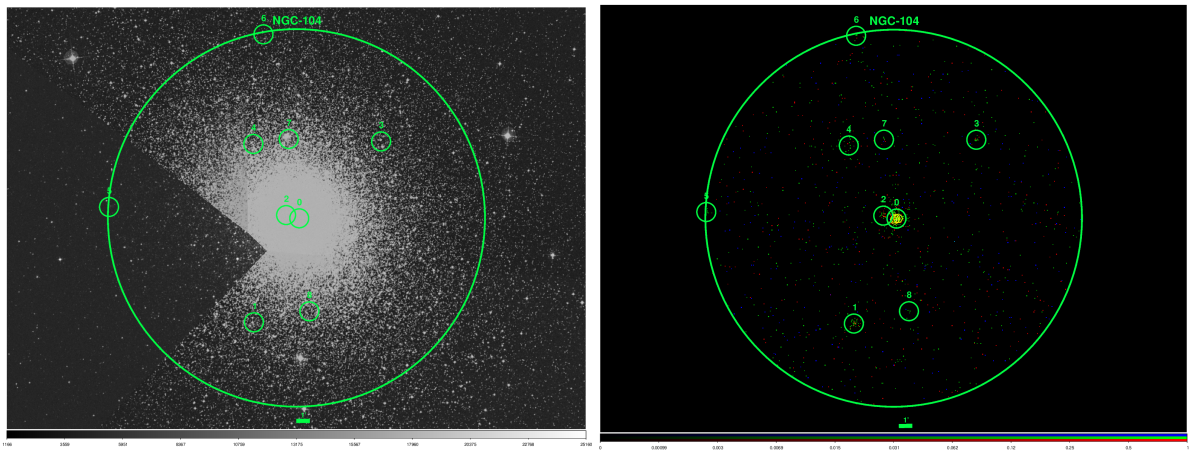

Fig. 4.20: Left: Optical image of NGC 104 (DSS total band)
Right: X-ray image of NGC 104 (similar to Figure 4.7), yellow circles mark the X-ray sources X9, X7 and X5 (from left to right).

With a mass of $(7.79 \pm 0.05) \cdot 10^5\,M_\odot$ (Baumgardt et al., 2018), 47 Tuc (NGC 104) is one of the most massive GCs in the Milky Way and the second brightest GC after ω Cen (Bhattacharya et al., 2017). Due to its large stellar density, 47 Tuc is predicted to have a very high stellar encounter rate. As a result, it is believed to occupy a high population of binaries with altered properties due to interactions with other stars or binaries. Bhattacharya et al., 2017 studied observations taken with the ACIS instrument onboard the Chandra observatory. They found 370 X-ray sources within the half-mass

radius of 47 Tuc, with the better part of the sources being located in the core. A comparison of the Chandra observations with HST data enabled the identification of 61 chromospherically active binaries (Grindlay et al., 2001, Edmonds et al., 2003a), 42 CVs, 6 companions to radio MSPs (Edmonds et al., 2003a), a quiescent neutron star LMXB (Edmonds et al., 2002b) and a candidate black hole binary (Bahramian et al., 2017a). In addition, studies of Parkes radio telescope observations lead to the discovery of 25 radio MSPs in 47 Tuc (Manchester et al., 1990, Ridolfi et al., 2016). The three most luminous sources in an energy range between 0.5 and 6.0 keV are 47 Tuc X9 ($L = 1151.9^{+13.2}_{-13.1} \cdot 10^{30}\,\mathrm{erg\,s^{-1}}$), X7 ($L = 1027.9^{+8.0}_{-6.7} \cdot 10^{30}\,\mathrm{erg\,s^{-1}}$) and X5 ($L = 574.2^{+6.1}_{-5.8} \cdot 10^{30}\,\mathrm{erg\,s^{-1}}$) (Bhattacharya et al., 2017). They are marked by yellow circles in the X-ray image (Figure 4.20). Bahramian et al., 2017a confirmed X9 as an UCXB with indications of a white dwarf donor and suggest that it is the first identified black hole UCXB in the Milky Way (Bahramian et al., 2017b). According to Bogdanov et al., 2016, X7 and X5 are quiescent neutron star LMXBs.
Nine eRASS1 sources have been detected in the direction of 47 Tuc. As apparent from Figure 4.20, 47 Tuc exhibits bright X-ray emission in the central GC region. However, due to the large half-mass-radius of 47 Tuc ($R_{\mathrm{m,47\,Tuc}} = 2.79'$), the bright central region appears much smaller than the source extraction region of five half-mass-radii (in contrast to the previously discussed GCs with bright central emission). 47 Tuc's most luminous X-ray sources X9, X7 and X5 are all concentrated within this bright region. Source 0 is the only eRASS1 source in the direction of 47 Tuc that has been classified as a GC source. It encompasses the bright central region, including the X-ray binaries X9, X7 and X5. Therefore it can be concluded that source 0 represents the combined X-ray emission of multiple sources in the GC core, including the emission of X9, X7 and X5.

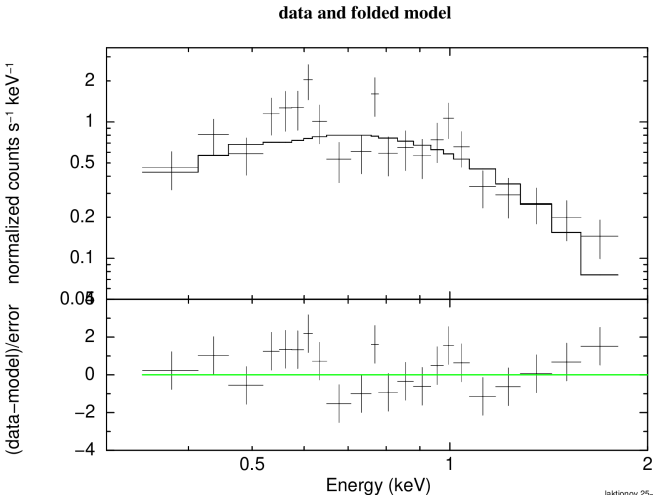

Fig. 4.21: Spectrum of NGC-104-0.

The spectrum of source 0 is displayed in Figure 4.21. Interestingly, it only covers energies up to 2 keV and is therefore the currently softest GC source. Hence, a blackbody model has been fitted onto the spectrum.
The soft nature of source 0 raises the question, whether it is actually a foreground star. To exclude this possibility, a 2mass near-infrared color-magnitude diagram has been created for 47 Tuc (see Figure 4.22), using data from the 2mass Vizier catalogue (Cutri, 2003).

The diagram displays the source population in a $5R_{\mathrm{m}}$ region in the direction of 47 Tuc (blue dots), as well as the fore- and background source population (orange dots). The fore- and background source data has been extracted from a same-sized region in a distance of $35R_{\mathrm{m}}$ from the GC center (towards smaller RA). A SkyMapper optical

color-magnitude has not been created, since no SkyMapper optical counterpart has been identified for source 0. The 2mass near-infrared counterpart of source 0 is marked by a green cross in Figure 4.22. It is located in the red giant branch of 47 Tuc. Therefore it can be concluded that source 0 is a GC source.

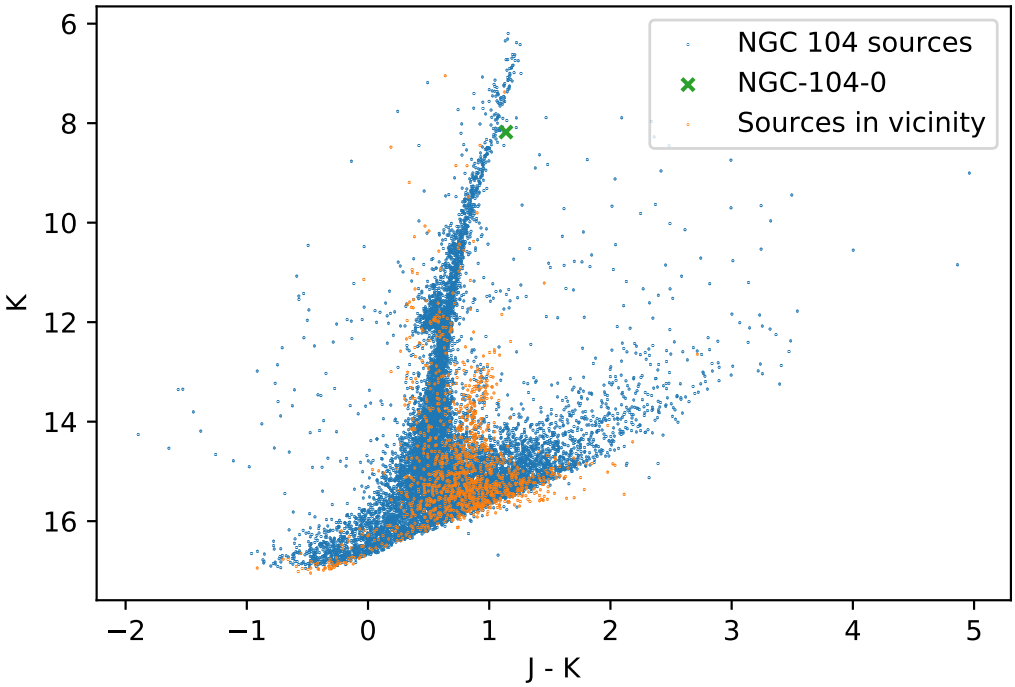

Fig. 4.22: 2mass near IR color-magnitude diagram (K over J-K) of NGC 104. Blue dots (NGC 104 sources) represent the 2mass sources within $5R_{\mathrm{m}}$ of the GC. Orange dots (Sources in vicinity) represent the 2mass sources in a circle with radius $5R_{\mathrm{m}}$ in a distance of $35R_{\mathrm{m}}$ to the GC center (towards smaller RA).

Messier 4

With a distance of 1.73 kpc to the Sun (Bassa et al., 2004), M4 (NGC 6121) is the nearest out of all GCs. Although it has a relatively low stellar encounter rate, it contains a binary star system with a pulsar companion *PSR B1620-26*. The pulsar orbits a $\sim 0.3\,\mathrm{M}_{\odot}$ white dwarf with a period of 191 days. Bassa et al., 2004 studied Chandra ACIS-S3 observations of M4 and found 12 X-ray sources within the core. 19 more X-ray sources are located inside the half-mass radius. Using HST data, they identified optical counterparts for 16 of these sources and classified 12 as chromospherically active binaries, 2 (possibly 3) as CVs and one as a MSP. The 8 most luminous sources have been marked by yellow circles in the X-ray image (Figure 4.23). *PSR B1620-26* has been marked by an orange circle. Bassa et al., 2004 have shown that the brightest X-ray source (a CV, source 1 in Figure 4.23) is variable.
The eRASS source selection in the direction of M4 yielded 5 results. All detections

coincide with noticeable X-ray emission, but only source 64 has been classified as a GC source that is luminous enough for further analysis. With 261.90 counts, it is by far the brightest X-ray source in the field. It has been classified as a type 2 detecion. In contrast to the previously discussed type 2 GC sources, detection 64 coincides with bright emission in the optical image (Figure 4.23). As apparent from Figure 4.23, the previously identified X-ray sources (including *PSR B1620-26*) are positioned not far from the GC center. However, the central GC region does not display bright X-ray emission. Similarly to ω Cen, this can be explained by the small core density of M4 ($\log \rho_c = 3.63\,M_\odot/pc^3$) (Baumgardt et al., 2018).

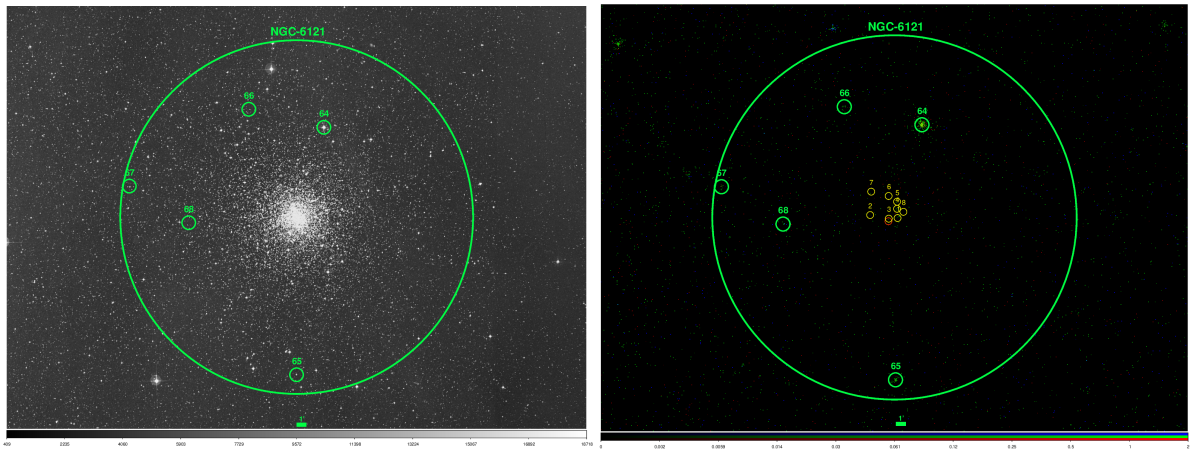

Fig. 4.23: Left: Optical image of NGC 6121 (DSS total band)
Right: X-ray image of NGC 6121 (similar to Figure 4.7), yellow circles mark an AB and a CV/AB candidate, orange circles mark CVs.

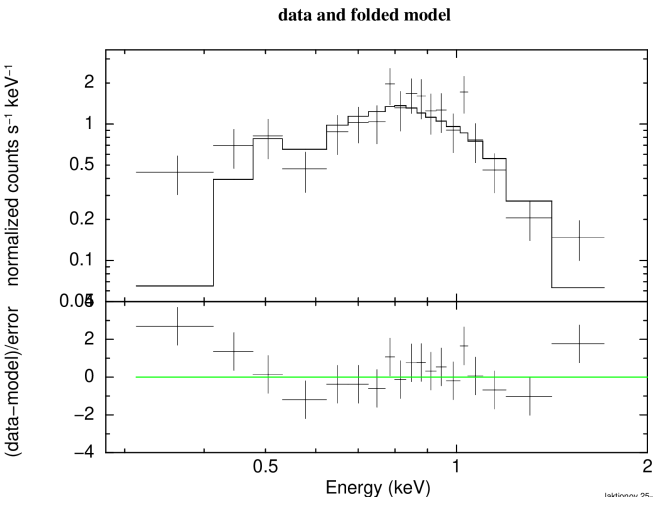

Fig. 4.24: Spectrum of NGC-6121-64.

The spectrum of source 64 is displayed in Figure 4.24. Like source 0 in 47 Tuc, it only covers energies up to 2 keV. Due to the soft nature of the source, a blackbody model has been fitted onto the spectrum.
For source 64, a 2mass near-infrared counterpart, as well as a SkyMapper optical counterpart was identified. To verify that source 64 is not a foreground star, a 2mass near-infraded color-magnitude diagram (see Figure 4.25) and a SkyMapper optical color-magnitude diagram (see Figure 4.26) were created for M4.

Similarly to the near-infrared color-magnitude diagram of 47 Tuc (Figure 4.22), the fore- and background sources have been marked by orange dots in both plots.

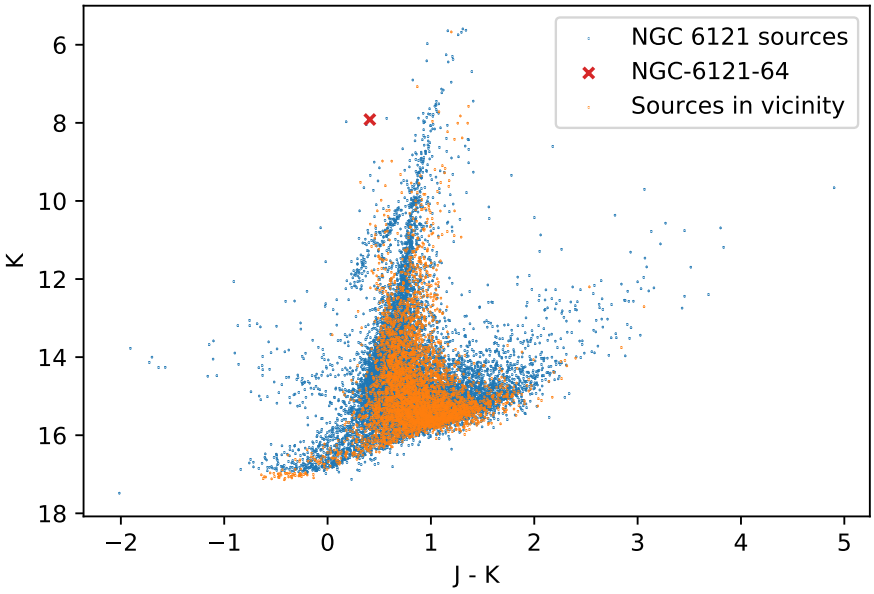

Fig. 4.25: 2mass near IR color-magnitude diagram (K over J-K) of NGC 6121 (similar to Figure 4.22).

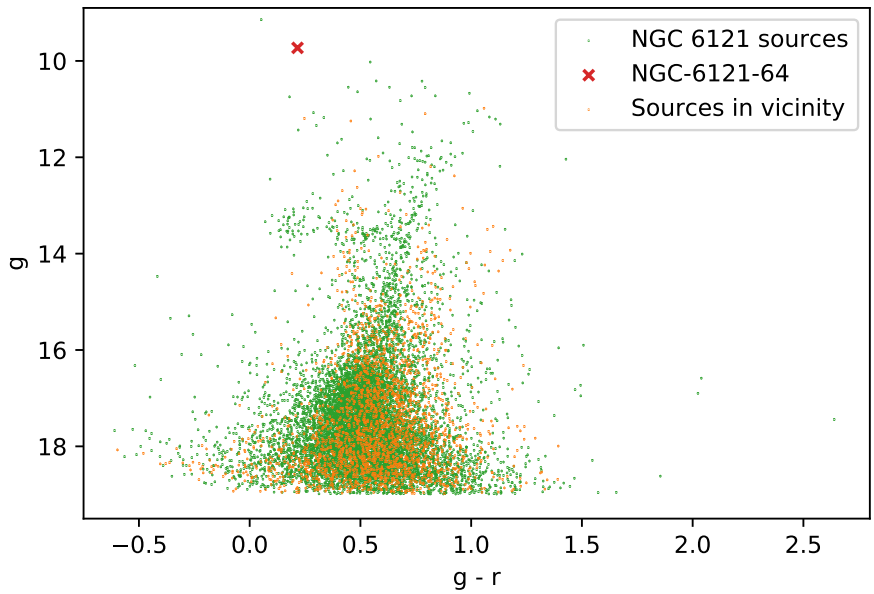

Fig. 4.26: SkyMapper optical color-magnitude diagram (g over g-r) of NGC 6121. Green dots (NGC 6121 sources) represent the SkyMapper sources within $5R_{\mathrm{m}}$ of the GC. Orange dots (Sources in vicinity) represent the SkyMapper sources in a circle with radius $5R_{\mathrm{m}}$ in a distance of $35R_{\mathrm{m}}$ to the GC center (towards smaller RA).

The counterpart of source 64 has been marked by a red cross. In both diagrams, the counterpart does not fit into the distribution of the GC sources. Instead, it lies in a region with lower g and $g - r$, indicating that it is a foreground star.

NGC 4372

NGC 4372 is a very low metallicity GC ([FE/H] = -2.09) located in a distance of 5.8 kpc to the Sun (Servillat et al., 2008). Kaluzny et al., 1993 studied optical observations of NGC 4372 and found that it contains 19 variable stars, out of which one is consistent with a $P = 0.4$ d eclipsing CV. Using the HR1 instrument of the ROSAT observatory, 9 X-ray sources have been detected in the direction of NGC 4372 (Johnston et al., 1996). None of these sources is located within the GC's half-mass-radius and they do not coincide with the variable stars. Servillat et al., 2008 studied XMM-Newton observations of NGC 4372 and found 10 X-ray sources in their field of view. Most of these detections are consistent with the sources found by Johnston et al., 1996. They are marked by yellow circles in the X-ray image (Figure 4.27).

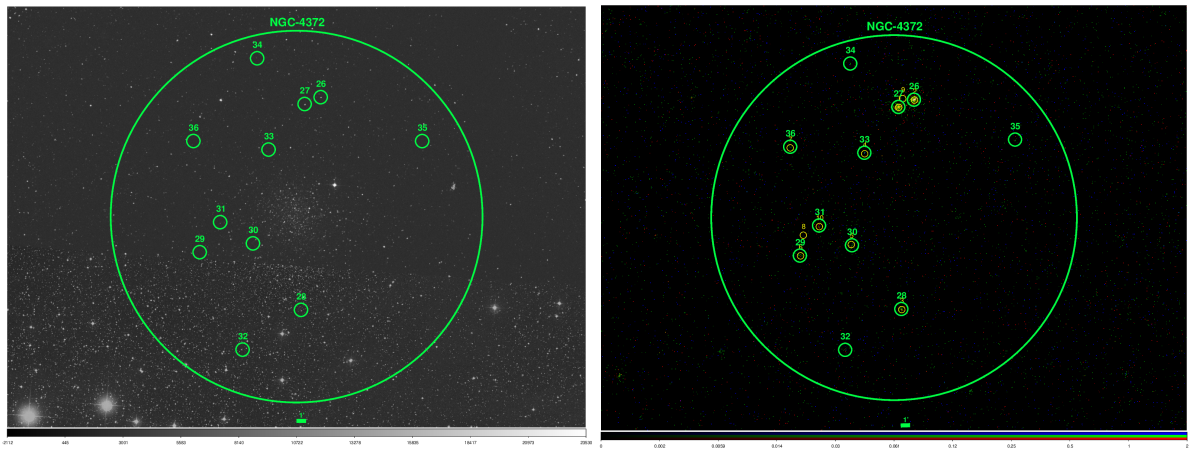

Fig. 4.27: Left: Optical image of NGC 4372 (DSS total band)
Right: X-ray image of NGC 4372 (similar to Figure 4.7).

11 eRASS1 sources have been detected in the direction of NGC 4372. Most of these sources coincide with noticeable emission in Figure 4.27. However, only source 26 and 27 have been classified as GC sources that are luminous enough for further analysis. With 477.02 and 447.81 counts, respectively, they are much brighter than the other detections and are positioned in close proximity to each other. As apparent from Figure 4.27, they are consistent with the positions of source 1 and 2 from the XMM-Newton study of Servillat et al., 2008. In addition, they coincide with emission in the optical image (Figure 4.27). The detections 28, 29, 30, 31, 33 and 36 also coincide with one of the sources from the study of Servillat et al., 2008. Similarly to ω Cen and M4, NGC 4372 does not display bright central emission. Likewise, this can be attributed to the small core density of NGC 4372 ($\log \rho_c = 1.98\,M_\odot/pc^3$) (Baumgardt et al., 2018).
Table 4.6 summarizes the radii, masses and core densities of the analyzed GCs and whether they display bright central emission (BCR). The GCs with $\log \rho_c \geq 4.60\,M_\odot/pc^3$

exhibit bright central emission, while the GCs with $\log \rho_c \leq 3.63\,M_\odot/pc^3$ do not. For Terzan 2 (which exhibits bright central emission) no data was available on the mass and core density in the catalogue provided by Baumgardt et al., 2018. However, according to Djorgovski, 1993, Terzan 2 has a core radius of $R_c \simeq 0.09\,pc$ and a star density of $\rho_c \simeq 10^4\,L_\odot/pc^3$.

GC ID	R_c [pc]	R_m [pc]	m [$M_\odot$]	$\log \rho_c$ [$M_\odot/pc^3$]	BCR
Liller 1	0.06	1.57	$(6.66 \pm 1.17) \cdot 10^5$	7.85	Yes
NGC 1851	0.15	3.09	$(3.02 \pm 0.04) \cdot 10^5$	6.57	Yes
NGC 6441	0.42	3.37	$(1.23 \pm 1.17) \cdot 10^5$	5.40	Yes
47 Tuc	0.49	5.62	$(7.79 \pm 0.05) \cdot 10^5$	5.31	Yes
NGC 2808	0.68	3.22	$(7.42 \pm 0.05) \cdot 10^5$	4.60	Yes
NGC 6121	0.66	4.20	$(9.69 \pm 0.26) \cdot 10^4$	3.63	No
ω Cen	4.22	10.04	$(3.55 \pm 0.03) \cdot 10^6$	3.22	No
NGC 4372	4.82	9.19	$(2.49 \pm 0.25) \cdot 10^5$	1.98	No

Tab. 4.6: Overview of the GC's core radii R_c, half-mass radii R_m, masses m and core densities ρ_c (Baumgardt et al., 2018). BCR = bright central region.

The spectra of source 26 and source 27 are displayed in Figure 4.28 and Figure 4.29, respectively. They display similar characteristics and are both very soft, only covering energies up to 2 keV. Blackbody models have been fitted onto the spectra in both cases. As apperent from Table 4.5, the resulting parameters are nearly identical.
Due to their soft nature, it must be verified that detection 26 and 27 are no foreground sources. For both detections, 2mass and SkyMapper counterparts have been identified. Therefore, similarly to the 47 Tuc and M4 diagrams, a 2mass near-infrared color-magnitude diagram (Figure 4.30), as well as a SkyMapper optical color-magnitude diagram (Figure 4.31) has been created for NGC 4372. The counterparts of source 26 are marked by a red cross, the counterparts of source 27 by a green/blue cross. They appear to be part of the red giant branch of NGC-4372 (see Figure 4.30). Therefore it can be concluded that they are located within NGC 4372.

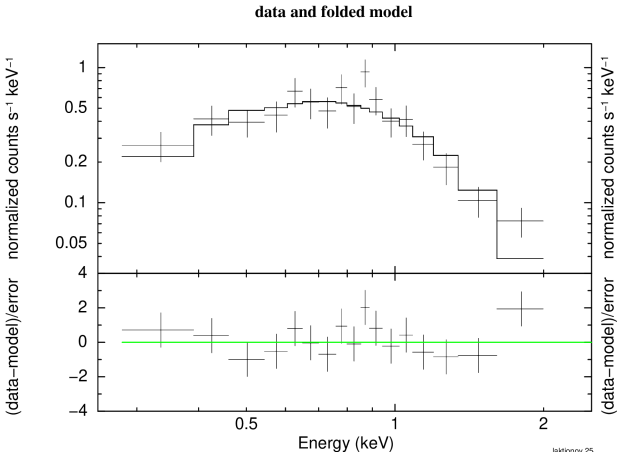

Fig. 4.28: Spectrum of NGC-4372-26.

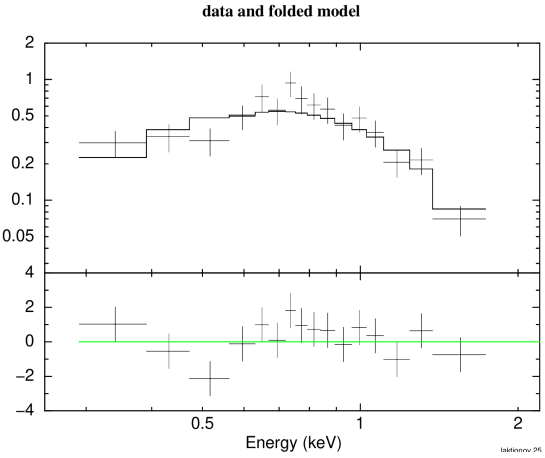

Fig. 4.29: Spectrum of NGC-4372-27.

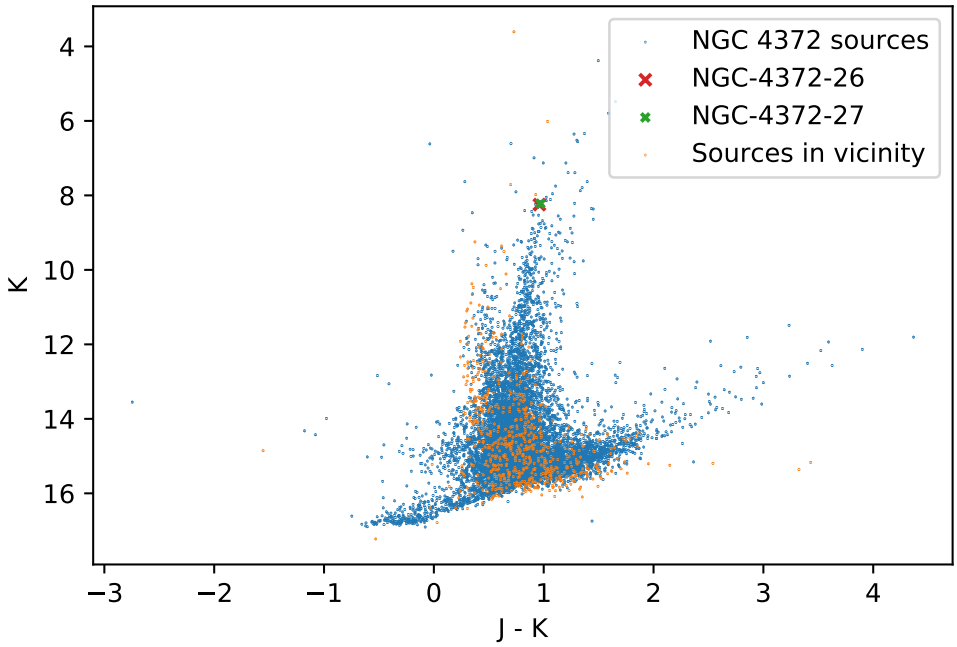

Fig. 4.30: 2mass near IR color-magnitude diagram (K over J-K) of NGC 4372 (similar to Figure 4.22).

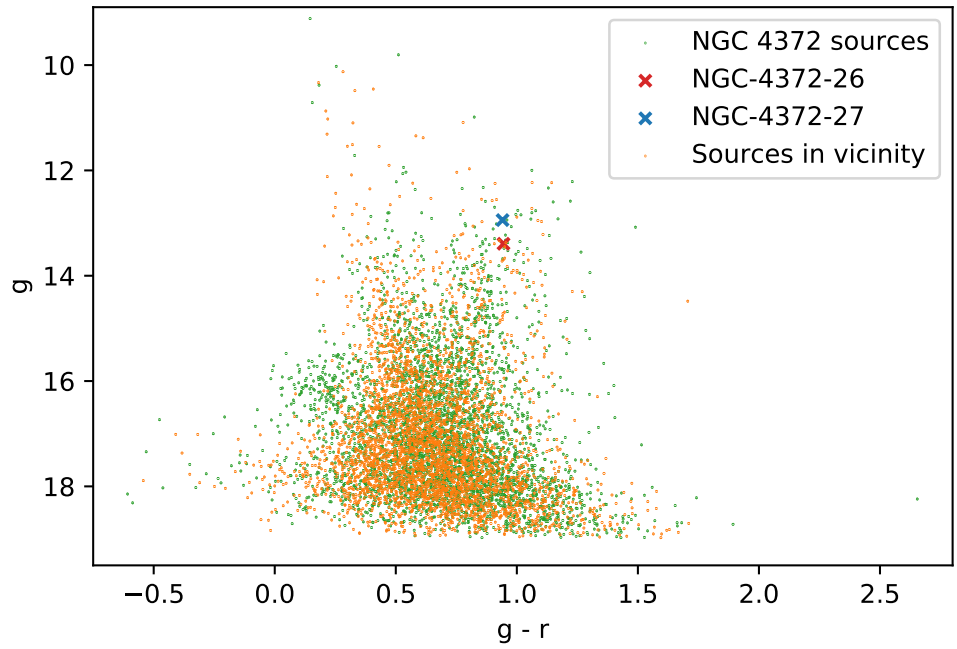

Fig. 4.31: SkyMapper optical color-magnitude diagram (g over g-r) of NGC 4372 (similar to Figure 4.26).

GC	Source	Nature
NGC 2808	C1	CV
NGC 2808	C3	CV
NGC 2808	C4	CV
NGC 2808	C5	CV
ω Cen	11b	
ω Cen	13a	CV
ω Cen	13c	CV
ω Cen	22c	fbCV?
ω Cen	24c	CV
ω Cen	31a	fbCV?
ω Cen	32f	RGB/SGB-a
ω Cen	34b	RGB/SGB-a
ω Cen	41d	CV
ω Cen	43h	CV?
ω Cen	44e	qLMXB
ω Cen	54b	fbCV?
ω Cen	54h	CV
ω Cen	73a	
ω Cen	94a	CH star
NGC 6441	A	binary MSP
NGC 6441	B	binary MSP
NGC 6441	C	MSP
NGC 6441	D	MSP
M4	1	CV
M4	2	CV
M4	3	AB
M4	4	CV/AB
M4	5	
M4	6	
M4	7	fg.
M4	8	AB

Tab. 4.7: Probable nature of previously detected X-ray sources. fbCV stands for faint blue CV, RGB/SGB-a for red giant branch / subgiant branch star and fg. for foreground source (Bassa et al., 2004; Freire et al., 2008; Henleywillis et al., 2018; Servillat et al., 2008).

5 Conclusion

The eROSITA data analysis yielded interesting results. During the eRASS1 scan of the celestial sphere, 113 X-ray sources were detected in the direction of the Milky Way's GCs. The cross-matching with catalogues at other wavelengths enabled counterpart identification for most of these sources. The acquired data was then used to create distance-magnitude, color-magnitude and magnitude-magnitude diagrams and lead to the classification of 6 foreground stars, as well as numerous stellar sources and background candidates. Furthermore, hardness ratio - count rate diagrams revealed that except for 16 sources, the detections were too faint for further analysis. A comparison of the source distribution with power-law and plasma temperature models yielded that the standard bands of eROSITA are not useful for an analysis based on hardness ratios prior to an adjustment for better comparability.
The 16 remaining sources, which are much brigher than the rest, are located in the direction of 9 GCs: Liller 1, Terzan 2, NGC 1851, NGC 2808, Omega Centauri, NGC 6441, 47 Tucanae, Messier 4 and NGC 4372. These GCs were selected for a more detailed study. Within this study, the 16 bright sources were marked in eRASS1 X-ray images and DSS optical images of their host GC. The images revealed, that only 6 out of the 9 GCs exhibit bright central X-ray emission. It has been discovered that the 3 other GCs (Omega Centauri, Messier 4 and NGC 4372) have much larger core radii than the rest. The absence of bright central emission can therefore be explained by the reduced stellar density. The GC images have also shown that the 16 bright sources are rather extended than point-like. For 6 detections, the source position coincides with the bright central region of the GC. Hence it can be concluded that the detections represent the combined X-ray emission of multiple sources in the GC core. Furthermore, 5 bright detections are located in close proximity to the GC core. It is possible that the high stellar density in the central GC region triggered multiple detections. This indicates that the resolution of the eRASS1 survey is insufficient to identify single X-ray sources, and that the detections encompass the emission of an area with multiple X-ray sources. Outside of the central GC region, 5 sources coincided with noticeable emission in the X-ray images.
A search for previously detected X-ray sources in the analyzed GCs has been conducted. All GCs except NGC 4372 are known to host at least one X-ray binary in their core. Despite containing multiple X-ray binaries in the core, Omega Centauri and Messier 4 don't exhibit bright central emission. In case of Omega Centauri, only 3 previously known sources coincide with eRASS1 detections; 0 in case of Messier 4. Those results are consistent with the conclusion that the resolution of eRASS1 is insufficient for the detection of most point-like GC X-ray sources.
Lastly, a spectral analysis has been carried out with Xspec for 10 of the bright sources. The source spectra were fitted by blackbody and powerlaw models. The resulting fit

parameters, e.g. the temperature kT, can be used to further constrain the nature of the detected sources. 4 sources had noticeably softer spectra than the rest. Their counterparts were marked in optical and near-infrared color-magnitude diagrams of their host GCs to verify their GC membership. It was concluded that 3 sources are indeed GC members, while one source is likely a foreground star.
Further analysis is required to confidently determine the nature of the detected sources. There is a good chance that the ongoing eROSITA All-Sky Survey will deliver important new detections and insights in the coming years.

6 Tables with Globular Cluster and Source Parameters

No.	ID	RA [h:m:ss]	DE [°:':"]	R_{sun} [kpc]	R_{gc} [kpc]	R_c [']	R_m [']
1	NGC 104	00 24 05.2	-72 04 51	4.3	7.3	0.37	2.79
2	NGC 288	00 52 47.5	-26 35 24	8.1	11.4	1.42	2.22
3	NGC 362	01 03 14.3	-70 50 54	8.3	9.2	0.17	0.81
4	NGC 1261	03 12 15.3	-55 13 01	16.0	17.9	0.39	0.75
5	Pal 1	03 33 23.0	+79 34 50	9.7	15.9	0.32	0.48
6	AM 1	03 55 02.7	-49 36 52	119.1	120.5	0.12	0.50
7	Eridanus	04 24 44.5	-21 11 13	80.8	85.8	0.25	0.40
8	Pal 2	04 46 05.9	+31 22 51	26.9	34.8	0.24	0.67
9	NGC 1851	05 14 06.3	-40 02 50	12.2	16.8	0.08	0.52
10	NGC 1904	05 24 10.6	-24 31 27	12.6	18.5	0.16	0.80
11	NGC 2298	06 48 59.2	-36 00 19	10.6	15.6	0.34	0.78
12	NGC 2419	07 38 08.5	+38 52 55	82.3	89.6	0.35	0.73
13	Pyxis	09 07 57.8	-37 13 17	38.5	40.5	1.38	1.35
14	NGC 2808	09 12 02.6	-64 51 47	9.3	10.9	0.26	0.76
15	E 3	09 20 59.3	-77 16 57	4.2	7.6	1.87	2.06
16	Pal 3	10 05 31.4	+00 04 17	89.4	92.6	0.48	0.66
17	NGC 3201	10 17 36.8	-46 24 40	5.1	8.9	1.45	2.68
18	Pal 4	11 29 16.8	+28 58 25	99.6	102.2	0.55	0.54
19	NGC 4147	12 10 06.2	+18 32 31	18.8	20.9	0.10	0.43
20	NGC 4372	12 25 45.4	-72 39 33	4.9	6.9	1.75	3.90
21	Rup 106	12 38 40.2	-51 09 01	20.6	18.0	1.00	1.10
22	NGC 4590	12 39 28.0	-26 44 34	10.1	10.0	0.69	1.55
23	NGC 4833	12 59 35.0	-70 52 29	5.9	6.9	1.00	2.41
24	NGC 5024	13 12 55.3	+18 10 09	18.4	18.9	0.37	1.11
25	NGC 5053	13 16 27.0	+17 41 53	16.2	16.8	2.25	3.50
26	NGC 5139	13 26 45.9	-47 28 37	5.1	6.3	2.58	4.18
27	NGC 5272	13 42 11.2	+28 22 32	10.0	11.9	0.50	1.12
28	NGC 5286	13 46 26.5	-51 22 24	10.7	8.2	0.29	0.69
29	AM 4	13 55 50.1	-27 10 22	29.2	24.8	0.42	0.42
30	NGC 5466	14 05 27.3	+28 32 04	16.6	16.9	1.96	2.25
31	NGC 5634	14 29 37.3	-05 58 35	25.3	21.3	0.21	0.54
32	NGC 5694	14 39 36.5	-26 32 18	33.9	28.3	0.06	0.33
33	IC 4499	15 00 18.5	-82 12 49	18.4	15.4	0.96	1.50
34	NGC 5824	15 03 58.5	-33 04 04	31.3	25.1	0.05	0.36

No.	ID	*RA* [h:m:ss]	*DE* [°:':"]	R_{sun} [kpc]	R_{gc} [kpc]	R_c [']	R_m [']
35	Pal 5	15 16 05.3	-00 06 41	22.6	18.0	2.90	2.96
36	NGC 5897	15 17 24.5	-21 00 37	12.7	7.6	1.96	2.11
37	NGC 5904	15 18 33.8	+02 04 58	7.3	6.1	0.40	2.11
38	NGC 5927	15 28 00.5	-50 40 22	7.4	4.5	0.42	1.15
39	NGC 5946	15 35 28.5	-50 39 34	12.3	7.1	0.08	0.69
40	BH 176	15 39 07.3	-50 03 02	15.2	9.4		
41	NGC 5986	15 46 03.5	-37 47 10	10.3	4.7	0.63	1.05
42	Lynga 7	16 11 03.0	-55 18 52	7.0	4.2		
43	Pal 14	16 11 04.9	+14 57 29	72.2	67.3	1.10	1.15
44	NGC 6093	16 17 02.5	-22 58 30	8.7	3.1	0.15	0.65
45	NGC 6121	16 23 35.5	-26 31 31	2.2	6.0	0.83	3.65
46	NGC 6101	16 25 48.6	-72 12 06	15.1	11.0	1.15	1.71
47	NGC 6144	16 27 14.1	-26 01 29	10.1	3.4	0.94	1.62
48	NGC 6139	16 27 40.4	-38 50 56	10.5	3.9	0.14	0.82
49	Terzan 3	16 28 40.1	-35 21 13	26.4	18.9	1.18	1.30
50	NGC 6171	16 32 31.9	-13 03 13	6.3	3.3	0.54	2.70
51	1636-283	16 39 25.5	-28 23 52	7.6	2.0		
52	NGC 6205	16 41 41.5	+36 27 37	7.0	8.3	0.88	1.49
53	NGC 6229	16 46 58.9	+47 31 40	29.3	28.7	0.13	0.37
54	NGC 6218	16 47 14.5	-01 56 52	4.7	4.6	0.66	2.16
55	NGC 6235	16 53 25.4	-22 10 38	9.7	2.7	0.36	0.84
56	NGC 6254	16 57 08.9	-04 05 58	4.3	4.6	0.86	1.81
57	NGC 6256	16 59 32.6	-37 07 17	9.3	2.3	0.02	0.85
58	Pal 15	17 00 02.4	-00 32 31	43.6	36.9	1.21	1.21
59	NGC 6266	17 01 12.6	-30 06 44	6.7	1.8	0.18	1.23
60	NGC 6273	17 02 37.7	-26 16 05	8.5	1.5	0.43	1.25
61	NGC 6284	17 04 28.8	-24 45 53	14.3	6.6	0.07	0.78
62	NGC 6287	17 05 09.4	-22 42 29	8.4	1.6	0.26	0.75
63	NGC 6293	17 10 10.4	-26 34 54	8.8	1.5	0.05	0.91
64	NGC 6304	17 14 32.5	-29 27 44	6.0	2.2	0.21	1.41
65	NGC 6316	17 16 37.4	-28 08 24	11.5	3.7	0.17	0.71
66	NGC 6341	17 17 07.3	+43 08 11	8.1	9.5	0.23	1.09
67	NGC 6325	17 17 59.2	-23 45 57	9.4	1.9	0.03	0.94
68	NGC 6333	17 19 11.8	-18 30 59	8.3	1.7	0.58	0.95
69	NGC 6342	17 21 10.2	-19 35 14	9.1	1.9	0.05	0.88
70	NGC 6356	17 23 35.0	-17 48 47	14.6	7.0	0.23	0.74
71	NGC 6355	17 23 58.6	-26 21 13	7.1	1.2	0.05	0.87
72	NGC 6352	17 25 29.2	-48 25 22	5.6	3.3	0.83	2.00
73	IC 1257	17 27 08.5	-07 05 35	24.5	17.3		
74	Terzan 2	17 27 33.4	-30 48 08	9.5	1.6	0.03	1.52
75	NGC 6366	17 27 44.3	-05 04 36	3.6	4.9	1.83	2.63
76	Terzan 4	17 30 38.9	-31 35 44	8.9	1.1		
77	HP 1	17 31 05.2	-29 58 54	7.2	0.9	0.03	3.10

No.	ID	*RA* [h:m:ss]	*DE* [°:':"]	R_{sun} [kpc]	R_{gc} [kpc]	R_c [']	R_m [']
78	NGC 6362	17 31 54.8	-67 02 53	7.5	5.1	1.32	2.18
79	Liller 1	17 33 24.5	-33 23 20	10.5	2.6	0.06	0.45
80	NGC 6380	17 34 28.0	-39 04 09			0.34	0.75
81	Terzan 1	17 35 47.8	-30 28 11	6.5	1.5	0.04	3.82
82	Ton 2	17 36 10.5	-38 33 12	7.9	1.4	0.54	1.08
83	NGC 6388	17 36 17.0	-44 44 06	11.5	4.4	0.12	0.67
84	NGC 6402	17 37 36.1	-03 14 45	8.7	3.8	0.83	1.29
85	NGC 6401	17 38 36.9	-23 54 32	7.5	0.9	0.25	1.91
86	NGC 6397	17 40 41.3	-53 40 25	2.2	6.0	0.05	2.33
87	Pal 6	17 43 42.2	-26 13 21	6.7	1.4	0.66	1.06
88	NGC 6426	17 44 54.7	+03 10 13	19.9	13.8	0.26	0.96
89	Djorg 1	17 47 28.3	-33 03 56	9.2	1.4	0.50	1.26
90	Terzan 5	17 48 04.9	-24 48 45	8.0	0.6	0.18	0.83
91	NGC 6440	17 48 52.6	-20 21 34	8.0	1.2	0.13	0.58
92	NGC 6441	17 50 12.9	-37 03 04	9.7	2.1	0.11	0.64
93	Terzan 6	17 50 46.4	-31 16 31	7.5	0.6	0.05	0.44
94	NGC 6453	17 50 51.8	-34 35 55	10.9	3.1	0.07	0.37
95	UKS 1	17 54 27.2	-24 08 43	7.5	0.8	0.15	0.86
96	NGC 6496	17 59 02.0	-44 15 54	11.6	4.4	1.05	1.87
97	Terzan 9	18 01 38.8	-26 50 23	7.8	0.6	0.03	0.78
98	Djorg 2	18 01 49.1	-27 49 33	13.8	5.8	0.33	0.83
99	NGC 6517	18 01 50.6	-08 57 32	10.5	4.1	0.06	0.62
100	Terzan 10	18 02 57.4	-26 04 00	8.4	0.8		
101	NGC 6522	18 03 34.1	-30 02 02	7.0	1.1	0.05	1.04
102	NGC 6535	18 03 50.7	-00 17 49	6.8	3.9	0.42	0.77
103	NGC 6528	18 04 49.6	-30 03 21	7.4	0.8	0.09	0.43
104	NGC 6539	18 04 49.8	-07 35 09	7.9	3.0	0.54	1.67
105	NGC 6540	18 06 08.6	-27 45 55	3.5	4.5	0.03	0.24
106	NGC 6544	18 07 20.6	-24 59 51	2.5	5.5	0.05	1.77
107	NGC 6541	18 08 02.2	-43 42 20	7.4	2.1	0.30	1.19
108	NGC 6553	18 09 15.6	-25 54 28	4.7	3.3	0.55	1.55
109	NGC 6558	18 10 18.4	-31 45 49	6.4	1.8	0.03	1.61
110	IC 1276	18 10 44.2	-07 12 27	9.3	3.6	1.08	2.35
111	Terzan 12	18 12 15.8	-22 44 31			0.83	0.84
112	NGC 6569	18 13 38.9	-31 49 35	8.5	1.1	0.37	1.33
113	NGC 6584	18 18 37.7	-52 12 54	13.0	6.5	0.59	0.80
114	NGC 6624	18 23 40.5	-30 21 40	7.9	1.2	0.06	0.82
115	NGC 6626	18 24 32.9	-24 52 12	5.7	2.5	0.24	1.56
116	NGC 6638	18 30 56.2	-25 29 47	8.2	1.5	0.26	0.66
117	NGC 6637	18 31 23.2	-32 20 53	8.2	1.5	0.34	0.83
118	NGC 6642	18 31 54.3	-23 28 35	7.6	1.6	0.10	0.73
119	NGC 6652	18 35 45.7	-32 59 25	9.4	2.2	0.07	0.65
120	NGC 6656	18 36 24.2	-23 54 12	3.2	5.0	1.42	3.26

No.	ID	RA [h:m:ss]	DE [°:':"]	R_{sun} [kpc]	R_{gc} [kpc]	R_c [']	R_m [']
121	Pal 8	18 41 29.9	-19 49 33	12.4	5.2	0.40	0.57
122	NGC 6681	18 43 12.7	-32 17 31	8.7	2.0	0.03	0.93
123	NGC 6712	18 53 04.3	-08 42 22	6.7	3.5	0.94	1.37
124	NGC 6715	18 55 03.3	-30 28 42	26.2	18.6	0.11	0.49
125	NGC 6717	18 55 06.2	-22 42 03	7.1	2.4	0.08	0.68
126	NGC 6723	18 59 33.2	-36 37 54	8.6	2.6	0.94	1.61
127	NGC 6749	19 05 15.3	+01 54 03	7.7	4.9	0.77	1.10
128	NGC 6752	19 10 51.8	-59 58 55	3.9	5.3	0.17	2.34
129	NGC 6760	19 11 12.1	+01 01 50	7.3	4.8	0.33	2.18
130	NGC 6779	19 16 35.5	+30 11 05	9.9	9.5	0.37	1.16
131	Terzan 7	19 17 43.7	-34 39 27	23.0	15.8	0.61	0.97
132	Pal 10	19 18 02.1	+18 34 18	5.8	6.4	0.81	0.99
133	Arp 2	19 28 44.1	-30 21 14	27.6	20.4	1.59	1.91
134	NGC 6809	19 39 59.4	-30 57 44	5.3	3.9	2.83	2.89
135	Terzan 8	19 41 45.0	-34 00 01	25.4	18.5	1.00	1.00
136	Pal 11	19 45 14.4	-08 00 26	12.6	7.6	2.00	1.49
137	NGC 6838	19 53 46.1	+18 46 42	3.8	6.7	0.63	1.65
138	NGC 6864	20 06 04.8	-21 55 17	18.4	12.4	0.10	0.47
139	NGC 6934	20 34 11.6	+07 24 15	15.2	12.4	0.25	0.60
140	NGC 6981	20 53 27.9	-12 32 13	16.8	12.7	0.54	0.88
141	NGC 7006	21 01 29.5	+16 11 15	40.7	38.0	0.24	0.38
142	NGC 7078	21 29 58.3	+12 10 01	10.2	10.3	0.07	1.06
143	NGC 7089	21 33 29.3	-00 49 23	11.4	10.3	0.34	0.93
144	NGC 7099	21 40 22.0	-23 10 45	7.9	7.0	0.06	1.15
145	Pal 12	21 46 38.8	-21 15 03	18.7	15.5	0.20	1.28
146	Pal 13	23 06 44.4	+12 46 19	26.3	27.2	0.48	0.46
147	NGC 7492	23 08 26.7	-15 36 41	25.2	24.3	0.83	1.22

Tab. 6.1: In this table, the known GCs in the Milky Way are displayed, including their spatial parameters RA (right ascension), DE (declination), R_{sun} (distance to the sun) and R_{gc} (distance to the Galactic center), as well as their radii R_c (core radius) and R_m (half-mass radius) Harris, 1997.

ID	GC	RA	DE	Counts	CR	Classif.
0	NGC-104	6.01045	-72.081343	309.84	1.45	1
1	NGC-104	6.193281	-72.209354	40.57	0.19	
2	NGC-104	6.063142	-72.077341	23.68	0.11	
3	NGC-104	5.683919	-71.986363	15.11	0.07	
4	NGC-104	6.193581	-71.989684	15.52	0.08	
5	NGC-104	6.772195	-72.065881	7.92	0.04	
6	NGC-104	6.152301	-71.854696	10.16	0.05	
7	NGC-104	6.052508	-71.98366	7.63	0.04	
8	NGC-104	5.969386	-72.195936	5.04	0.03	
9	NGC-288	13.11793	-26.618476	13.92	0.09	
10	NGC-362	15.814956	-70.850321	21.39	0.09	
11	NGC-362	15.860055	-70.894985	18.79	0.08	
12	NGC-362	15.925262	-70.892285	6.36	0.03	
13	NGC-1851	78.525579	-40.043859	27730.91	80.28	1
14	NGC-1851	78.511218	-40.061486	545.61	1.55	2
15	NGC-1851	78.475587	-40.038142	29.65	0.08	
16	NGC-1851	78.581367	-40.043111	792.05	2.17	2
17	NGC-1904	81.065358	-24.523198	22.38	0.11	
18	NGC-1904	81.05034	-24.527989	7.84	0.04	
19	NGC-2298	102.26851	-35.98469	9.75	0.05	
20	NGC-2808	138.009602	-64.866835	22869.09	46.15	1
21	NGC-2808	138.06621	-64.921485	16.05	0.03	
22	NGC-2808	138.12897	-64.855335	128.97	0.27	
23	E-3	139.99515	-77.348301	9.99	0.02	
24	NGC-3201	154.311284	-46.384985	7.75	0.05	
25	NGC-4147	182.509954	18.511449	6.54	0.06	
26	NGC-4372	186.299652	-72.45027	477.02	1.05	2
27	NGC-4372	186.392735	-72.462313	447.81	0.98	2
28	NGC-4372	186.413226	-72.822174	49.13	0.12	
29	NGC-4372	187.009762	-72.720542	22.21	0.06	
30	NGC-4372	186.695993	-72.705793	28.08	0.07	
31	NGC-4372	186.887932	-72.668372	23.05	0.05	
32	NGC-4372	186.760394	-72.891431	17.5	0.05	
33	NGC-4372	186.602687	-72.541872	10.76	0.03	
34	NGC-4372	186.667164	-72.38221	10.79	0.03	
35	NGC-4372	185.708286	-72.525785	8.21	0.02	
36	NGC-4372	187.040188	-72.526109	8.75	0.02	
37	Rup-106	189.705034	-51.215808	64.74	0.25	
38	Rup-106	189.678854	-51.135967	7.2	0.03	
39	NGC-4590	189.869213	-26.751461	34.58	0.19	
40	NGC-5053	199.137554	17.969105	15.91	0.1	
41	NGC-5053	199.33122	17.751229	13.26	0.08	
42	NGC-5053	198.972197	17.668631	10.92	0.07	
43	NGC-5053	199.240588	17.439077	6.05	0.04	

ID	GC	RA	DE	Counts	CR	Classif.
44	NGC-5053	198.984221	17.611303	10.06	0.07	
45	NGC-5139	202.170112	-47.463716	358.61	1.4	2
46	NGC-5139	201.467216	-47.318415	49.23	0.18	
47	NGC-5139	201.337601	-47.43874	25.75	0.09	
48	NGC-5139	201.865332	-47.319172	23.25	0.09	
49	NGC-5139	201.271279	-47.345284	15.76	0.06	
50	NGC-5139	201.50944	-47.551047	14.17	0.06	
51	NGC-5139	201.726004	-47.483467	15.86	0.06	
52	NGC-5139	201.757976	-47.681836	13.45	0.05	
53	NGC-5139	201.970307	-47.664407	11.66	0.05	
54	NGC-5139	202.110569	-47.525262	10.72	0.04	
55	NGC-5139	201.213762	-47.430584	13.94	0.06	
56	NGC-5139	201.547483	-47.623945	13.21	0.05	
57	NGC-5139	202.03581	-47.557776	10.11	0.04	
58	NGC-5139	201.587633	-47.487388	10.8	0.04	
59	NGC-5139	202.061564	-47.490082	10.22	0.04	
60	NGC-5139	201.726492	-47.307639	8.08	0.03	
61	NGC-5897	229.31385	-21.158421	8.01	0.05	
62	NGC-5897	229.371862	-21.105255	6.9	0.04	
63	NGC-6093	244.266266	-22.975365	13.78	0.08	
64	NGC-6121	245.845533	-26.370862	261.9	1.76	2
65	NGC-6121	245.898163	-26.796493	43.41	0.29	
66	NGC-6121	245.99001	-26.3398	11.09	0.07	
67	NGC-6121	246.220261	-26.47164	12.38	0.08	
68	NGC-6121	246.106011	-26.534862	8.71	0.06	
69	NGC-6101	246.858293	-72.153387	27.99	0.12	
70	NGC-6101	246.51819	-72.147411	16.42	0.08	
71	NGC-6101	246.093349	-72.166419	10.26	0.04	
72	NGC-6101	246.778339	-72.158169	9.13	0.04	
73	NGC-6139	246.918906	-38.848908	10.64	0.06	
74	NGC-6235	253.39067	-22.196166	9.94	0.06	
75	NGC-6266	255.302766	-30.113141	37.86	0.26	
76	NGC-6304	258.547976	-29.532422	24.05	0.16	
77	NGC-6316	259.209547	-28.106962	8.06	0.07	
78	NGC-6352	261.301551	-48.353419	7.99	0.05	
79	NGC-6352	261.335997	-48.493582	11.4	0.08	
80	Terzan-2	261.886976	-30.800186	3395.22	26.98	1
81	Terzan-2	261.828809	-30.828867	78.52	0.63	2
82	Terzan-2	261.904339	-30.789197	1006.82	7.54	2
83	HP-1	263.021485	-30.059424	14.61	0.1	
84	HP-1	262.942196	-30.17662	11.18	0.08	
85	NGC-6362	263.157328	-67.056886	8.7	0.05	
86	Liller-1	263.351048	-33.38702	1949.05	17.57	1
87	Liller-1	263.36708	-33.398725	827.27	7.34	2

ID	GC	RA	DE	Counts	CR	Classif.
88	Liller-1	263.317705	-33.369826	587.25	4.56	2
89	Terzan-1	264.075288	-30.739275	6.95	0.05	
90	Terzan-1	263.75479	-30.686434	9.5	0.08	
91	NGC-6388	264.070659	-44.736356	26.06	0.19	
92	NGC-6397	265.17485	-53.671455	43.78	0.3	
93	NGC-6397	265.364996	-53.801883	14.33	0.09	
94	NGC-6397	265.139433	-53.729447	14.95	0.1	
95	NGC-6397	265.055579	-53.842408	9.26	0.06	
96	NGC-6397	265.394441	-53.533943	12.52	0.08	
97	NGC-6397	265.347509	-53.771235	8.77	0.06	
98	NGC-6397	265.327472	-53.648326	8.59	0.06	
99	NGC-6397	265.326156	-53.820663	8.54	0.06	
100	Djorg-1	266.969094	-33.118842	8.56	0.06	
101	NGC-6441	267.550853	-37.050205	9823.52	78.62	1
102	NGC-6441	267.58289	-37.052753	44.36	0.34	
103	NGC-6441	267.597932	-37.033209	23.52	0.18	
104	NGC-6496	269.927432	-44.226659	9.83	0.07	
105	NGC-6541	272.008784	-43.713592	24.93	0.25	
106	NGC-6584	274.715166	-52.22798	9.47	0.08	
107	NGC-6723	284.735157	-36.674127	17.86	0.18	
108	NGC-6723	285.007391	-36.617677	16.25	0.16	
109	NGC-6752	287.513422	-59.926046	23.04	0.2	
110	NGC-6752	287.712526	-59.982708	13.58	0.1	
111	NGC-6752	287.517627	-60.050905	12.08	0.1	
112	NGC-2808	137.952352	137.952352	593.54	1.21	

Tab. 6.2: This table displays all eRASS1 sources that were found via the source selection (see section 4.1). It contains the source ID, the host GC, the right ascension RA, the declination DE, the total counts, the count rate CR and, if available, the classification type from Table 4.4 of each source. Detections without a classification type are either too faint for further analysis or have been classified as a foreground source or background candidate rather than a GC source.

Appendix

As mentioned in section 4.3, the eRASS sources were also cross-matched with the SkyMapper and 2mass infrared catalogues. The obtained counterparts were used to create color-magnitude diagrams. They are shown in Figure 6.2 in and Figure 6.1.

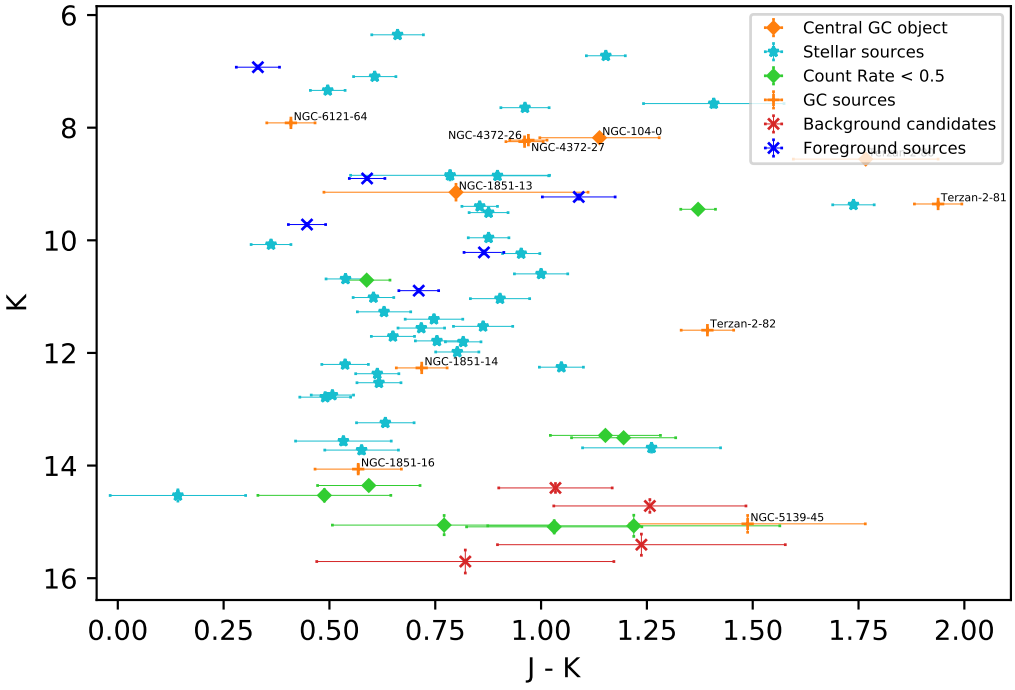

Fig. 6.1: Color-magnitude diagram (2mass band K over J-K).

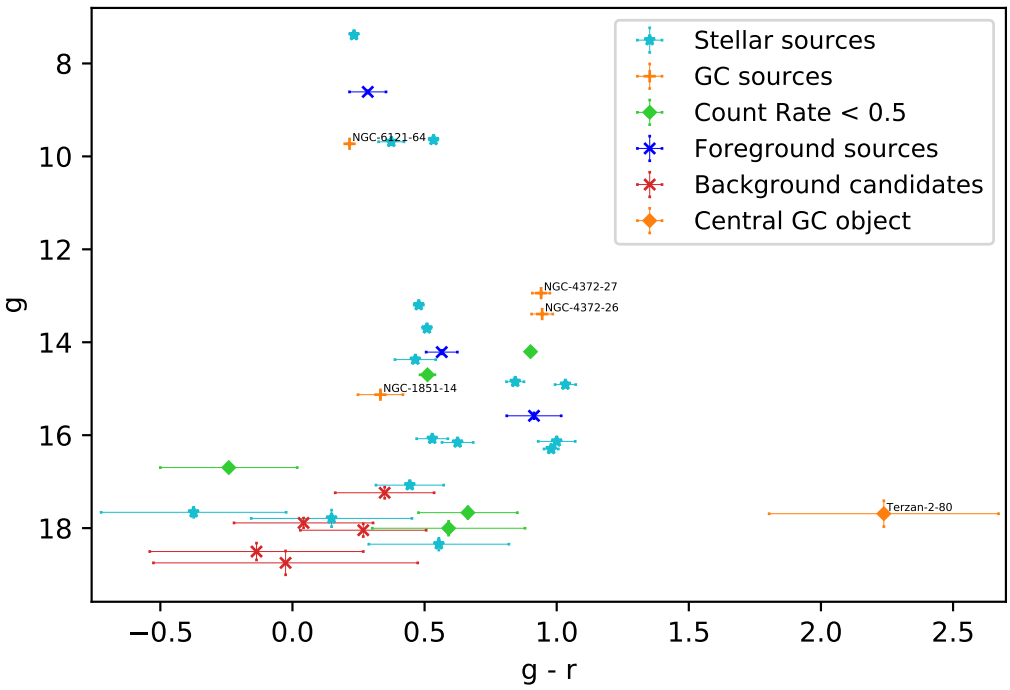

Fig. 6.2: Color-magnitude diagram (SkyMapper band g over g-r).

Acknowledgements

Many thanks to everyone who supported me during the work on this thesis! Without the help of my supervisor Manami Sasaki, and the assistance of Sara Saeedi, it would not have been possible to conduct this study. Thank you Manami for providing the interesting topic, your continuous support and your patience. Thank you Sara for helping out with the spectral analysis, the hardness ratio models and the overall collaboration. Thank you Jonathan Knies for providing the source-matching script *artemis*. And thank you Theresa Heindl for the mutual motivation and support!

This work is based on data from eROSITA, the primary instrument aboard SRG, a joint Russian-German science mission supported by the Russian Space Agency (Roskosmos), in the interests of the Russian Academy of Sciences represented by its Space Research Institute (IKI), and the Deutsches Zentrum fur Luft- und Raumfahrt (DLR). The SRG spacecraft was built by Lavochkin Association (NPOL) and its subcontractors, and is operated by NPOL with support from the Max-Planck Institute for Extraterrestrial Physics (MPE).
The development and construction of the eROSITA X-ray instrument was led by the Max Planck Institute for Extraterrestrial Physics (MPE), with contributions from the Dr. Karl Remeis-Observatory of the Friedrich-Alexander-University Erlangen Nuremberg, the University of Hamburg Observatory, the Leibniz Institute for Astrophysics Potsdam (AIP), and the Institute for Astronomy and Astrophysics of the University of Tübingen, with the support of DLR and the Max Planck Society. The Argelander Institute for Astronomy of the University of Bonn and the Ludwig-Maximilians-Universität Munich also participated in the science preparation for eROSITA.
The eROSITA data shown here were processed using the eSASS software system developed by the German eROSITA consortium.
This publication makes use of data products from the Wide-field Infrared Survey Explorer, which is a joint project of the University of California, Los Angeles, and the Jet Propulsion Laboratory/California Institute of Technology, funded by the National Aeronautics and Space Administration. This work has made use of data from the European Space Agency (ESA) mission Gaia (`https://www.cosmos.esa.int/gaia`), processed by the Gaia Data Processing and Analysis Consortium (DPAC, `https://www.cosmos.esa.int/web/gaia/dpac/consortium`). Funding for the DPAC has been provided by national institutions, in particular the institutions participating in the Gaia Multilateral Agreement.
This publication makes use of data products from the Two Micron All Sky Survey, which is a joint project of the University of Massachusetts and the Infrared Processing and Analysis Center/California Institute of Technology, funded by the National Aeronautics and Space Administration and the National Science Foundation. The na-

tional facility capability for SkyMapper has been funded through ARC LIEF grant LE130100104 from the Australian Research Council, awarded to the University of Sydney, the Australian National University, Swinburne University of Technology, the University of Queensland, the University of Western Australia, the University of Melbourne, Curtin University of Technology, Monash University and the Australian Astronomical Observatory. SkyMapper is owned and operated by The Australian National University's Research School of Astronomy and Astrophysics. The survey data were processed and provided by the SkyMapper Team at ANU. The SkyMapper node of the All-Sky Virtual Observatory (ASVO) is hosted at the National Computational Infrastructure (NCI). Development and support the SkyMapper node of the ASVO has been funded in part by Astronomy Australia Limited (AAL) and the Australian Government through the Commonwealth's Education Investment Fund (EIF) and National Collaborative Research Infrastructure Strategy (NCRIS), particularly the National eResearch Collaboration Tools and Resources (NeCTAR) and the Australian National Data Service Projects (ANDS).

Bibliography

About 2MASS (2006). IPAC. URL: https://old.ipac.caltech.edu/2mass/overview/about2mass.html (visited on 03/27/2021).

Amaro-Seoane, P. et al. (2013). "Mergers of multimetallic globular clusters: the role of dynamics". In: *Monthly Notices of the Royal Astronomical Society* 435 (1).809–821.

Arenou, F. et al. (2018). "Gaia Data Release 2. Catalogue validation". In: *Astronomy and Astrophysics* 616.A17.

Ashman, K. M. et al. (1992). "The formation of globular clusters in merging and interacting galaxies". In: *The Astrophysical Journal* 384.50–61.

Bahramian, A. et al. (2017a). In: *Monthly Notices of the Royal Astronomical Society* 467.2199.

Bahramian, A. et al. (2017b). "The ultracompact nature of the black hole candidate X-ray binary 47 Tuc X9". In: *Monthly Notices of the Royal Astronomical Society* 467.2.

Barmby, P. et al. (2001). "M31 Globular Clusters in the Hubble Space Telescope Archive. I. Cluster Detection and Completeleness". In: *The Astronomical Journal* 122 (5).2458–2468.

Bassa, C. et al. (2004). "X-ray sources and their optical counterparts in the globular cluster M4". In: *The Astrophysical Journal* 609.2.

Baumgardt, H. et al. (2018). "A catalogue of masses, structural parameters and velocity dispersion profiles of 112 Milky Way globular clusters". In: *Monthly Notices of the Royal Astronomical Society* 478.2.

Bekki, K. et al. (2003). "Formation of Omega Centauri from an ancient nucleated dwarf galaxy in the young Galactic disc". In: *Monthly Notices of the Royal Astronomical Society* 346.2.

Belli, B. M. et al. (1986). "Terzan 2". In: *IAU Circ.* 4174.1.

Benacquista, M. J. (2006). "Globular cluster structure". In: *Living Reviews in Relativity* 9 (1).2.

Bergh, van den et al. (2007). "Globular Clusters and Dwarf Spheroidal Galaxies". In: *Monthly Notices of the Royal Astronomical Society* 385 (1).385 (1.

Bhattacharya, S. et al. (2017). "Chandra studies of the globular cluster 47 Tucanae: A deeper X-ray source catalogue, five new X-ray counterparts to millisecond radio pulsars, and new constraints to r-mode instability window". In: *Monthly Notices of the Royal Astronomical Society* 472.3.

Bogdanov, S. et al. (2016). "Neutron star mass-radius constraints of the quiescent low-mass X-ray binaries X7 and X5 in the globular cluster 47 Tuc". In: *the Astrophysical Journal* 831.2.

Buonanno, R. et al. (1994). "The Stellar Population of the Globular Cluster M 3. I. Photographic Photometry of 10 000 Stars". In: *Astronomy and Astrophysics* 290.69–103.

Callanan, P. J. et al. (1995). "X-ray observations of NGC 1851 and the globular cluster LMXBs". In: *Monthly Notices of the Royal Astronomical Society* 273.1.

Caloi, V. et al. (2007). "NGC 6441: another indication of very high helium content in globular cluster stars". In: *Astronomy and Astrophysics* 463.3.

Carretta, E. et al. (2015). "The normal chemistry of multiple stellar populations in the dense globular cluster NGC 6093 (M 80)". In: *Astronomy and Astrophysics* 578.A116.

Cutri (2003). *2MASS All-Sky Catalog of Point Sources*. URL: `http://vizier.u-strasbg.fr/viz-bin/VizieR-3?-source=II/246/out` (visited on 03/23/2021).

Cutri, R. M. et al. (2012). *Explanatory Supplement to the WISE All-Sky Data Release Products*. URL: `https://wise2.ipac.caltech.edu/docs/release/allsky/expsup/sec6_3a.html` (visited on 03/27/2021).

Dai, S. et al. (2020). "Discovery of Millisecond Pulsars in the Globular Cluster Omega Centauri". In: *The Astrophysical Journal* 888.2.

Data Release DR2. Release documentation (2019). URL: `https://skymapper.anu.edu.au/data-release/` (visited on 03/27/2021).

Deutsch, E. W. et al. (1998). "The Probable Optical Counterpart of the Luminous X-Ray Source in NGC 6441". In: *The Astrophysical Journal* 493.775.

Djorgovski, S. (1993). "Structure and Dynamics of Globular Clusters". In: *eds. S.G Djorgovski & G. Meylan (San Francisco: ASP)*.

Edmonds, P. D. et al. (2002b). In: *The Astrophysical Journal* 564.L17.

Edmonds, P. D. et al. (2003a). In: *The Astrophysical Journal* 596.1177.

Egg, K. (2020). "X-ray Source Population Studies of Cen A (NGC 5128) with Chandra Data". In: *Friedrich-Alexander-Universität Erlangen-Nürnberg*.

Elmegreen, B. G. et al. (1999). "A Universal Formation Mechanism for Open and Globular Clusters in Turbulent Gas". In: *The Astrophysical Journal* 480 (2).235–245.

eROSITA (2021). High-Energy Astrophysics Group at MPE. URL: `https://www.mpe.mpg.de/eROSITA` (visited on 03/23/2021).

ESA (2013). *ESA Gaia home*. URL: `http://www.esa.int/Science_Exploration/Space_Science/Gaia` (visited on 10/23/2013).

ESO (2005). *Young and Exotic Stellar Zoo: ESO's Telescopes Uncover Super Star Cluster in the Milky Way*. URL: `https://web.archive.org/web/20070409105105/`

http://eso.org/outreach/press-rel/pr-2005/pr-08-05.html (visited on 03/17/2021).

Forbes, D. A. et al. (2010). "Accreted versus in situ Milky Way globular clusters". In: *Monthly Notices of the Royal Astronomical Society* 404.3.

Forbes, D. A. et al. (2018). "Globular cluster formation and evolution in the context of cosmological galaxy assembly: open questions". In: *Proc. R. Soc. A* 474.20170616.

Freire, P. C. C. et al. (2008). "Eight New Millisecond Pulsars in NGC 6440 and NGC 6441". In: *The Astrophysical Journal* 675.1.

Frenk, C. S. et al. (1980). "The ellipticities of Galactic and LMC globular clusters". In: *Monthly Notices of the Royal Astronomical Society* 286 (3).L39–L42.

Friedrich, P. (2019). *The Spectrum-Roentgen-Gamma mission will study the X-ray sky between 0.2 and 30 keV*. URL: https://physicsworld.com/a/german-russian-x-ray-telescope-takes-off-to-study-the-dark-universe/ (visited on 03/23/2021).

Frommert, H. et al. (2007). "Open Star Clusters". In: *SEDS. University of Arizona, Lunar and Planetary Lab.*

Gaia DR2 Passbands (2018). ESA/Gaia/DPAC. URL: https://www.cosmos.esa.int/web/gaia/iow_20180316 (visited on 03/27/2021).

Gratton, R. et al. (2019). "What is a Globular Cluster? An observational perspective". In: *The Astronomy and Astrophysics Review manuscript.*

Grindlay, J. E. et al. (2001). In: *Science* 292.2290.

Harris (1997). *Globular Clusters in the Milky Way*. URL: http://vizier.u-strasbg.fr/viz-bin/VizieR?-source=VII/202 (visited on 03/23/2021).

– (2001). *Star Clusters*. URL: https://faculty.virginia.edu/ASTR5610/lectures/globular_clusters/pop_tracers.html (visited on 04/12/2021).

Harris, W. E. (1991). "Globular cluster systems in galaxies beyond the Local Group". In: *Annual Review of Astronomy and Astrophysics* 29 (1).543–579.

Henleywillis, S. et al. (2018). "A Deep X-ray Survey of the globular cluster Omega Centauri". In: *Monthly Notices of the Royal Astronomical Society* 479.2.

Homer, L. et al. (2001). "The rapid burster in Liller 1: The Chandra X-ray position and a search for an infrared counterpart". In: *The astronomical journal* 122.

Homer, L. et al. (2002). "The Optical Identification of the X-ray Burster X1746-370 in the Globular Cluster NGC 6441 ". In: *The Astronomical Journal* 123.6.

Janes, K. (2000). "Star Clusters". In: *Encyclopedia of Astronomy and Astrophysics* p. 2.

Johnston, H. M. et al. (1996). In: *Astronomy and Astrophysics* 309.116.

Kaluzny, J. et al. (1993). In: *Monthly Notices of the Royal Astronomical Society* 264.785.

Lewin, W. H. G. et al. (1993). "X-Ray Bursts". In: *Space Science Reviews* 62.3-4.

Lindegren, L. et al. (2018). "Gaia Data Release 2. The astrometric solution". In: *Astronomy and Astrophysics* 616.A2.

Manchester, R. N. et al. (1990). In: *Nature* 345.598.

McClure, R. D. et al. (1990). "The Binary Nature of the Barium and CH Stars. III. Orbital Parameters". In: *The Astrophysical Journal* 352.

McLaughlin, D. E. et al. (1994). "The spatial structure of the M87 globular cluster system". In: *The Astronomical Journal* 422 (2).486–507.

Mereghetti, S. et al. (1995). "X-ray and radio observations of the globular cluster Terzan 2". In: *Astronomy and Astrophysics* 302.

Messier 80 (2017). The Hubble Heritage Team (AURA/STScI/NASA). URL: `https://www.nasa.gov/feature/goddard/2017/messier-80` (visited on 03/23/2021).

NASA's HEASARC Column Density Tool (2021). NASA's HEASARC: Tools. URL: `https://heasarc.gsfc.nasa.gov/cgi-bin/Tools/w3nh/w3nh.pl` (visited on 03/23/2021).

Parmar, A. M. et al. (1989). In: *Astronomy and Astrophysics* 222.96.

Piotto, G. (2009). "Observations of multiple populations in star clusters. The Ages of Stars, Proceedings of the International Astronomical Union". In: *IAU Symposium* 258.233–244.

Pooley, D. (2010). "Globular cluster x-ray sources". In: *Proceedings of the National Academy of Sciences of the United States of America* 107.16.

Predehl, P. et al. (2020). "The eROSITA X-ray telescope on SRG". In: *Astronomy and Astrophysics* 647.A1.

Ridolfi, A. et al. (2016). "Long-term observations of the pulsars in 47 Tucanae. I. A study of four elusive binary systems". In: *Monthly Notices of the Royal Astronomical Society* 462.3.

Ridolfi, A. et al. (2019). "Upgraded Giant Metrewave Radio Telescope timing of NGC 1851A: a possible millisecond pulsar-neutron star system". In: *Monthly Notices of the Royal Astronomical Society* 490.3.

Sandage, A. R. (1957). "Observational Approach to Evolution. III. Semiempirical Evolution Tracks for M67 and M3". In: *The Astrophysical Journal* 126.326.

Sanna, A. et al. (2017). "Discovery of a new accreting millisecond X-ray pulsar in the globular cluster NGC 2808". In: *Astronomy and Astrophysics* 598.A34.

Sansom, A. E. et al. (1993a). In: *Monthly Notices of the Royal Astronomical Society* 262.429.

– (1993b). "Detection of a 5.7-h period in the globular cluster X-ray source 4U 1746 – 371". In: *Monthly Notices of the Royal Astronomical Society* 262.2.

Saracino, S. et al. (2015). "GEMINI/GeMS observations unveil the structure of the heavily obscured globular cluster Liller 1". In: *The Astrophysical Journal* 806.2.

Sasaki, M. et al. (2018). "Deep XMM-Newton observations of the northern disc of M31". In: *Astronomy and Astrophysics* 620.A28.

Secker, J. (1992). "A Statistical Investigation into the Shape of the Globular cluster Luminosity Distribution". In: *Astronomical Journal* 104 (4).1472–1481.

Servillat, M. et al. (2008). "XMM-Newton observations of the Galactic globular clusters NGC 2808 and NGC 4372". In: *Astronomy and Astrophysics* 480.2.

SkyView (2021). *SkyView Query Form*. URL: `https://skyview.gsfc.nasa.gov/current/cgi/query.pl` (visited on 03/23/2021).

Talpur, J. (1997). "A Guide to Globular Clusters". In: *Keele University*.

Tauris, T. M. et al. (2006). "Chapter 16: Formation and evolution of compact stellar X-ray sources". In: *In Lewin, Walter; van der Klis, Michiel (eds.). Compact Stellar X-ray Sources* Cambridge Astrophysics Series. 39.

Wright, E. L. et al. (2010). "The Wide-field Infrared Survey Explorer (WISE): Mission Description and Initial On-orbit Performance". In: *The Astronomical Journal* 140.6.

Zurek, D. R. et al. (2009). "An ultracompact X-ray binary in the globular cluster NGC 1851". In: *The Astrophysical Journal* 699.1113-1118.

Eigenständigkeitserklärung

Hiermit erkläre ich, dass ich die vorliegende Arbeit selbstständig verfasst und dabei keine anderen als die angegebenen Quellen und Hilfsmittel verwendet habe.

.....	.....
Ort, Datum	Roman Laktionov